SELENOLOGY TODAY

➡ **Messier, Messier A and surrounding Mare Fecunditatis**

➡ **Crater depths from the Apollo era to the present**

➡ **Lunar domes classification and physical properties**

OLR GROUP.org
Geological Lunar Researches Group

Selenology Today is devoted to the publication of contributions in the field of lunar studies.

Manuscripts reporting the results of new research concerning the astronomy, geology, physics, chemistry and other scientific aspects of Earth's Moon are welcome.

Selenology Today publishes papers devoted exclusively to the Moon.

Reviews, historical papers and manuscripts describing observing or spacecraft instrumentation are considered.

SELENOLOGY TODAY #5
April 2007

Cover : Image taken by Gerardo Sbarufatti, Schmidt Cassegrain 200 mm f/10.

Selenology Today websites

http://digilander.libero.it/glrgroup/

http://www.selenologytoday.com/
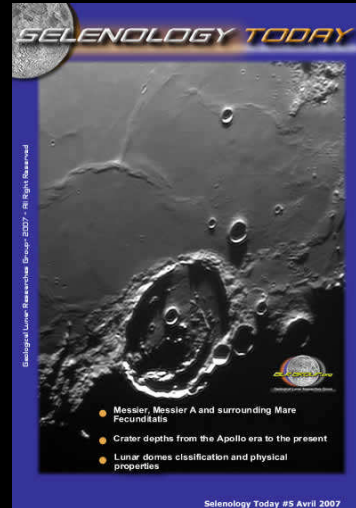
Messier, Messier A and surrounding Mare Fecunditatis

by Alexander Vandenbohede
Association for Lunar and Planetary Observers – Lunar Section

Abstract

Messier and Messier A (formerly called Pickering) form an interesting crater pair situated on the western part of Mare Fecunditatis. The shape of both craters is irregular resulting in intriguing changing views during a lunation. Also, both craters show highly asymmetrical ejecta deposits. Messier is centre of a butterfly-type of ray system and a comet-type ray system stretches from Messier A towards the border of the mare. Classic lunar observers had some very imaginative explanations for these characteristics. A low angle impact, however, is now generally thought to be the reason for the observed morphology of the Messier crater pair. The aim of the article is to overview the geology and morphology of the region. This is done using spacecraft and Earth-based images.

Introduction

Messier and Messier A are a remarkable crater pair situated on the western part of Mare Fecunditatis (figure 1). Messier is the eastern crater of the pair, Messier A the western crater. Messier has an oval shape with a diameter of 9 x 11 km and a depth of 1900 m. It is named after the famous French comet observer and author of the Messier catalogue of star clusters, nebulae, galaxies etc. Charles Messier (1730 – 1817). Messier A has a diameter of 11 x 13 km and a depth of 2250 m. Both craters fall in the category of small craters (less than 15 – 20 km). However, their shape is atypical for these small and in most cases simple bowl shaped craters. Also atypical is the shape of the ejecta deposits, which is highly asymmetrical. Messier features a butterfly-type of ray system with deposits towards the north and south of the crater. Messier A shows the well-know comet-type ray system with two major rays between the crater and the adjacent highland area. Because of these peculiar ejecta deposits, the ray system is under study in the International Bright Lunar Rays Project. First results of this were summarised by Dembowski (2003).

The geological map of the area (figure 1) indicates both craters of Copernican age (Elston, 1974). Towards the north and south of the craters low ropy ridges subradial to the craters are mapped (yellow, Cerr on map). Normally, this terrain is found axial-symmetric around an impact crater. Here, this zone is elongated north-south around both craters. The mare surface itself is of Imbrium age. West of Messier A is a system of low mare ridges. Two circular systems of mare ridges are present. These must be buried craters (so called ghost craters). North of Lubbock, there is a rille, part of the Rimae Goclenius. North-west of Messier A a small rima, Rima Messier, is visible. This is a delicate and difficult to observe feature. A dome is indicated just north of the small crater west of Rima Messier on Rükl's map.

Besides the interesting ejecta deposit, Messier and Messier A were also known

to the classic selenologists for their changing appearance throughout a lunation. These aspects were subject of much spirited discussion among them. The aim of this paper is to describe the different aspects of the crater pair (morphology, causes of the changing appearance, distribution and nature of the ejecta deposits) and to discus the formation mechanism of this all. This is done with imagery from different spacecraft orbiting the Moon and with Earth-based amateur images. The latter illustrate what an amateur lunar observer can see of the interesting geological story this part of the Moon has to offer.

Changing view of Messier and Messier A
Historical background

Schröter (1745-1816) was the first to draw attention to the curious variations in apparent shape and relative size of the crater pair under changing illumination. These variations were thoroughly confirmed by Gruithuisen (1774-1852). Also Webb (1807-1885), Neison (1849-1940) and Elger (1838-1897) have described their changing nature. Interestingly, Beer (1797-1850) and Mädler (1794-1874) never did so. They described them as "alike two peas in a pod" although they claimed to have inspected the formation no fewer than 300 times between 1829 and 1837. And although Beer and Mädler described the two as being alike, their map showed differences between them. Messier is drawn smaller than Messier A. Gruithuisen already noted this difference in diameter and he also draws Messier A larger than Messier. Interestingly, Schröter depicts Messier as the largest

of the two. Lohrman (1796-1840) draws Messier as an ellipse and Messier A as circle. According to Elger (1838-1897), Messier A is more triangular than Messier. W.H. Pickering (1858-1938) gave a nice description of the variations (from Sheenan and Dobbins, 2001):

"Sometimes one of these craters is the larger and sometimes the other. Sometimes they are triangular and sometimes elliptical in shape. When elliptical their major axes are sometimes parallel and sometimes perpendicular to one another. When the sun first rises on them they are of the same brilliance as the mare upon which they are situated, but three days later they both suddenly turn white, and remain so until the end of the lunation. When first seen the white areas are comparatively large, especially that surrounding Messier itself, but it gradually diminishes in size under the sun's rays."

The cause of all these changes was quite enigmatic and very few observers were convinced that both craters actually went through these seemingly chaotic changes. This was so until W.H. Pickering noticed in 1892 that the crater pair changes in the same way during every lunation. For instance, 5 and 9 days after local sunrise, the two craters look almost identical just like Beer and Mädler have described. W.H. Pickering thought that the cause for the alterations was the alternate evaporation and deposition of frost. Most of his contemporaries, however, were convinced that differences in lighting combined with peculiar topography were sufficient to explain the differences. A hint about this peculiar topography can be seen of the 1874 map of Julius Schmidt (1825-1884). Messier
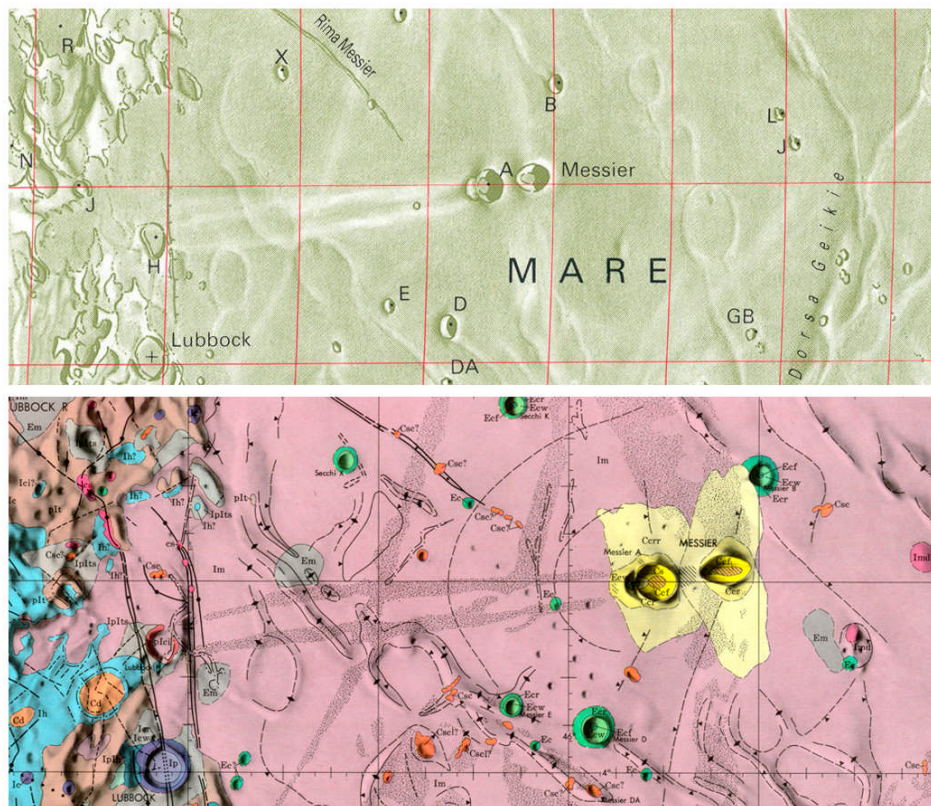
Figure 1 Localisation map (from Rükl, 1996) and geological map (from Elston, 1972).
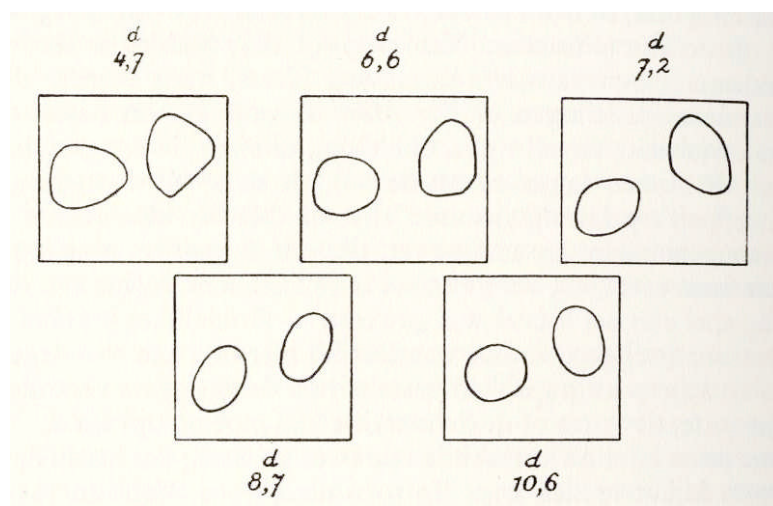

Figure 2 The changing shape of Messier A (right) and Messier (Wanders, 1949). The time indicates the number of days since sunrise over the crater pair.

is drawn as an ellipse with its long axis oriented east-west. Messier A is circular but with a crescent shaped wall along its western side. This topography is also visible on the map of Krieger (1865-1902). The change during a lunation is due to the fact that this crescent shaped wall becomes gradually invisible. During this process Messier A can be seen as circular, triangular and elliptical. Size changes are attributed to the fact that the space between Messier A and the crescent shaped wall is or is not filled with shadow. To conclude this historical overview of observations, it is quite remarkable that such observers as Beer and Mädler described the pair as equal. Most of their 300 observations were perhaps focused on the comet-like tail of Messier A and did they only occasionally observe the craters themselves?

Crater pair morphology

As was first indicated by W.H. Pickering, the observed variations are optical illusion originating in the peculiar morphology of the craters and the varying illumination during the course of a lunation. Messier A consists actually of two parts. This is very well visible on the Apollo 11 pictures (figure 4). The most brilliant part (further called Messier A2) overlaps a shallow elongated depression (further called Messier A1). Messier A1 which is visible west of the Messier A2 is the crescent shaped wall Schmidt and Krieger drew on their map. Messier is an elliptical crater whereby the eastern inner wall has a larger angle than the western wall.

Hill (1991) describes vividly with a set of beautiful drawings what happens when the sun rises over the pair. Under low early lighting Messier A1 is relatively bright against Messier A2 which is still filled with shadow. This gives Messier A its characteristic triangular shape. This brightness of A1 relative to A2 diminishes in function of the rising sun. Meanwhile the shadow in Messier A2 diminishes. Its western inner wall becomes bright but here two bright parts can be observed divided by a less bright zone. Thereafter Messier A1 becomes less visible and is almost lost against the immediate surroundings so that what remains of Messier A assumes the shape of a north-south oriented oval. According to the drawings of Wanders (1949) the triangular shape is visible until about 8 days after local sunrise. Under a high sun, Messier A is seen as a bright ellipse with a slightly less bright interior. During sunset over Messier A, the opposite happens. The Messier A1 is filled with shadow as is the western part of Messier A2 and a triangular shape is again visible. The western outer wall of Messier A2 is still visible so that these two shadows are clearly separated. As the sun sets further above Messier A, these two shadows merge, first in the middle, until there is one triangular shadow filling the interior of both parts of Messier A.

Clementine image (figure 5) shows very well the brightness difference between Messier A1 and Messier A2. The latter is very bright and looks undisturbed as can be expected from a geologically young impact crater. Messier A2 is difficult to distinguish it from the surrounding mare.

Messier itself remains elliptical in shape from sunrise to sunset. During sunrise, the shape of interior shadow is rounded but there is a less dark zone running
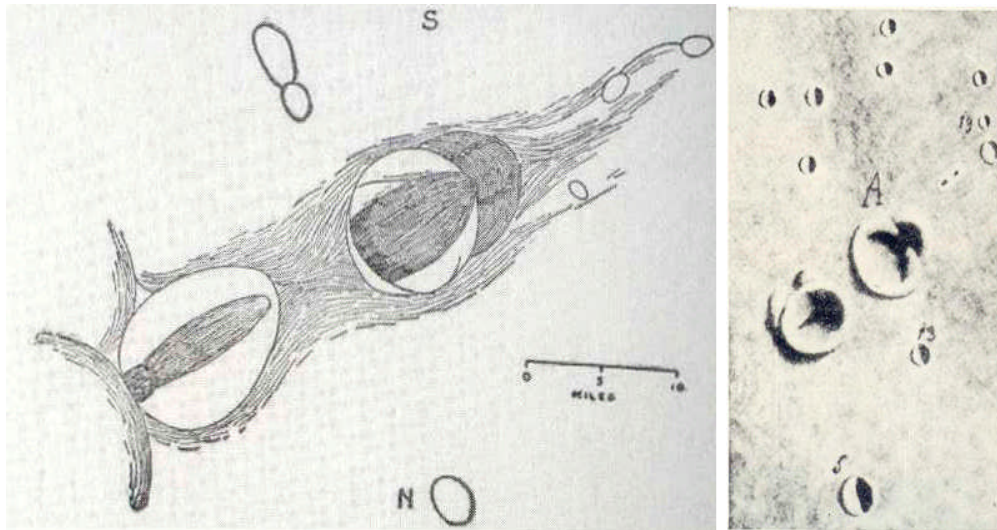
Figure 3 Left drawing is of W.H. Pickering made at Arequipa using the 13-inch Boyden refractor (Pickering, 1904). Notice the elongated inner dark zone in both craters. Also visible is a darker zone, west of Messier A. This is, as we now know, part of the older crater on which Messier A is super positioned. Right drawing is of Krieger (from, Wanders, 1949) showing very well the so-called 'crescent shaped wall'. Again this is the part of the older crater beneath Messier A. The zone between Messier A and this crescent shaped wall is filled with shadow resulting in a triangular shape.

Figure 4 Apollo 11 (upper row) and Apollo 15 (lower row) images of Messier and Messier A. The Apollo 11 images show very well the superposition of a younger above older impact crater morphology of Messier A. The older crater is clearly filled with material, most likely ejecta deposits coming from the younger impact. Messier itself is also interesting. Notice the very low eastern rim and the higher western rim. The slope of the eastern inner wall is noticeable larger than that of the western wall. This can all be explained by a low angle impact coming from the east. Apollo 15 images clearly show the east-west elongated flat floor of Messier.

towards the western wall. During sunset from a colongitude of about 120° in Hill's drawings, the transition between shadow and light has a distinct v-shape. The shape of these shadows thus indicates that Messier is not bowl-shaped but has a flat, east-west elongated floor. This can be well seen on the Apollo 15 image (figure 4). Figure 6 shows a number of observations with the 20 cm F15 Refractor of Beisbroek Public Observatory of the crater pair during sunrise.

Low angle impact

Messier and Messier A are both small craters (15-20 km). Such craters are relatively simple in comparison with larger ones. The walls are talus slopes rather than having coherent slump blocks forming terraces on the inner crater walls. Central peaks are generally absent. Obviously this is not the case for the Messier crater pair. Departures from circularity for small craters are due to structural control during excavation, post-impact modification, non-impact origin or low angles of impact (Guest and Greeley, 1977). Elongated craters, such as Messier, originate from certain conditions of impact or from endogenic processes. The former is the case for Messier and Messier A as also the presence of the ejecta deposits shows (see further). If the angle of impact is less than about 5° above the surface, the projectile may plough through the surface, producing an elongated crater. On impact, the projectile may even ricochet or break apart and produce a series of elongated craters. These craters normally have bilateral symmetry along the axis of the projectile's trajectory and

show a distinctive ejecta pattern. In profile, elongated craters produced in laboratory simulations by low-angle impact events are deeper at the up-range end and the rim on the down-range end is higher. This is exactly the case for Messier, considering a low angle impact coming from the east. The right Apollo 11 image on figure 4 hints that this is also the case for Messier A. Additionally, its formation and possible post-impact deformation must have been affected by the older crater on which it is superposed.

Ejecta deposit

The Messier crater pair features an interesting ejecta deposit. Best known is the comet tail like rays between Messier A and Lubbock H on the edge of the highlands to the west. This is a distance of about 105 km. Messier was actually named after the famous French comet hunter because of the resemblance. The comet tail consists of two major rays situated between Messier A and the highland area north of Lubbock. Both rays are approximately 6 km across at their widest point. The eastern parts of both rays are brighter than the western parts. This is normal since the impact came from the east and the brightness of the ejecta deposit thus will decrease from east to west. However, a system of mare ridges situated almost halfway between Messier A and the highlands also interfere. It is for instance noticeable that under a low sun (c = 327,7°), the rays can be observed without problem east of these mare ridges and are almost invisible west of it (figure 7). Under a higher sun, the western parts of the rays also become easily visible. It is very difficult to say
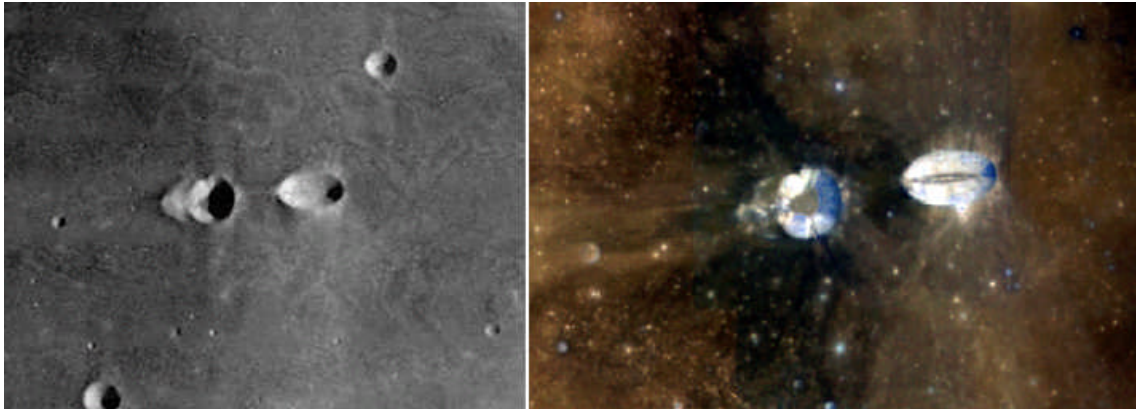
Figure 5 Lunar Orbiter (left) and Clementine shot of Messier and Messier A. The Lunar Orbiter image shows A1 very well. Notice the brightness difference between Messier or Messier A2 and the older Messier A1.

Figure 6 Observations of sunrise over Messier and Messier A photographed with the 20 cm F15 refractor of Beisbroek Public Observatory. A webcam in prime focus was used. Colongitudes are from left to right 327,7°, 339,9°, 346,6° and 352,1°. These are details of figure 7. The crescent-shaped wall west of Messier A is well visible in the first image thanks to the shadow west of it and the brightness of its eastern wall. Under a higher sun, the true nature of this "wall", being an older subdued crater, becomes visible. Notice how the brightness of the western inner wall of this older crater decreases.

where the rays end. This is first of all due to the fact that the brightness of the rays decreases with distance to Messier A but also because this happens in the lunar highlands. It is very difficult, even quite impossible, to follow the delicate distal parts of the rays in the bright highland area. Although the author had several times the impression that the rays could be followed in the highland area, images taken at the same time never confirmed this. Moreover, the geological map (figure 1) does not show continuation of ray material into the highlands. A ray of Taruntius also crosses the Messier A rays. Taruntius is also of Copernican age and it is difficult to say which deposit is the younger one. A second part of the ejecta deposits stretches north and south of Messier. Both components are quite different. The southern component is at it widest near the crater pair, stretching from the east wall of Messier A to the east wall of Messier. It becomes narrower south until it intermingles with other ray segments about 70 km south of Messier. The eastern edge of the ray is fairly straight whereas this is less the case for the western edge. This is most probably due to interference with low northwest-southeast oriented mare ridges. The northern component is about the same width as the southern component near the crater pair. The northern component, however, feathers out towards the north. The distal part of the northern ray looks fibrous with bright and darker parts. This is again due to interference of the ejecta deposit with mare ridges. This interaction can be well seen on figure 7. The distal part of the northern component intermingles with rays coming from Taruntius.

Schröter assumed that the famous comet tail deposit was formed around 1796. Now we know that the characteristics of the deposit are also due to the low-angle impact. Gault and Wedekind (1978) reported that the shape of an impact crater and its ejecta pattern depend on the angle at which a projectile strikes a target. They showed, using the Ames Vertical Gun Ballistic Range, that this shape and ejecta pattern does not change very much until the impact angle is less than 45°. At shallower angles the craters becomes increasingly elongated in the direction of projectile travel. If the impact angle is less than 15°, the ejecta pattern becomes elongated in the down range direction. In the up range direction, a "forbidden zone" exists where no ejecta appears. For impact angles of just a few degrees, the rays go sideways only, producing a butterfly-wing pattern. Interestingly Gault and Wedekind (1978) were able to mimic the Messier crater pair's weird ejecta pattern. They showed that low angle impacts (5° and less) produce a butterfly-wing pattern like found around Messier.

If part of the projectile ricocheted downrange this formed to two long rays like those found west of Messier A.

The strange morphology of Messier A (which was subdivided in parts A1 and A2) must also be the result of the oblique impact. Such unexpected morphologies are visible, in the experiments of Gault and Wedekind (1978).

Also, Wilhelms (1987) discusses the Messier pair as atypical craters.

Colour imaging and albedo

Own observations

Figure 8 shows an enhanced colour image of Mare Fecunditatis and surroundings whereas figure 9 shows a more detailed enhanced colour image of the Messier crater pair. These show Mare Fecunditatis as a patchwork of blue and different shades of yellow to red. The blue patches, for instance along the north-eastern rim is what Pieters (1978) called the hDWA unit. Pieters (1978) identified different units in the maria based on spectral reflectance studies. The hDWA unit represents medium titanium basalts sampled by Luna 16 on Mare Fecunditatis. The main part of Mare Fecunditatis belongs to the mIG unit which is a low titanium basalt type, hence its redder colour. The ejecta deposits of the Messier crater pair are clearly more redder than its surroundings.

Clementine UVVIS images

Figure 8 also shows a Clementine colour ratio image. The rays close to Messier and Messier A are green whereas the distal parts are green to yellow. The rays are very well recognisable against the patchwork of red and blue colours which make up the basalts of Mare Fecunditatis. Andre et al. (1979) used Apollo orbital X-ray fluorescence data to show that Messier A excavated magnesium-rich mare basalts from beneath less-magnesium rich surface units in Mare Fecunditatis. Hawke et al. (2004) used Earth-based spectral and radar data and Clementine UVVIS images to study composition and maturity of ejecta deposits. One of the deposits described by these authors is the Messier/Messier A deposit. They showed that in the spectrum obtained from the interior of Messier, an extremely deep ferrous absorption band is present. Further, the mafic assemblage is dominated by high-Ca pyroxene. This indicates a fresh mare composition. Also, radar images show that the interiors are enriched in blocks (0.5 – 10 m) and smaller fragments (0.01– 0.5 m). Hawke et al. (2004) showed that the rays west of Messer A exhibits FeO values (16–17 w%) slightly less than those of the adjacent mare deposits (17–18 w%). The TiO_2 values of the rays (3–4 w%) are lower than those of the nearby mare units (4–6 w%). This all means that the comet-type rays are dominated by relatively immature mare basalts. However, the FeO and TiO_2 values indicate that the basaltic material in these rays has a composition slightly different from those of the adjacent mare units. The radar and optical maturity images also show that the comet-type rays are relatively immature whereas the nearby mare is mature. The rays are enriched in fragments in the 1 to 50 cm size range but not enriched in blocks (0.5–1 m). Also, Hawke et al. (2004) showed that the ray south of Messier is dominated by mare basalt. FeO (17–18 w%) and TiO_2 (4–6 w%) is similar to those determined for the adjacent mare surface. No highland material is present in the Messier and Messier A rays. They are composed entirely of basaltic material. Nevertheless, these rays are bright. This is due to the fact that they are immature.

Albedo map

Pohn and Wildey (1970) made a

02/05/2006 2015 UT
col = 327,7°

03/05/2006 2015 UT
col = 339,9°

02/06/2006 2030 UT
col = 346,6°

04/05/2006 2015 UT
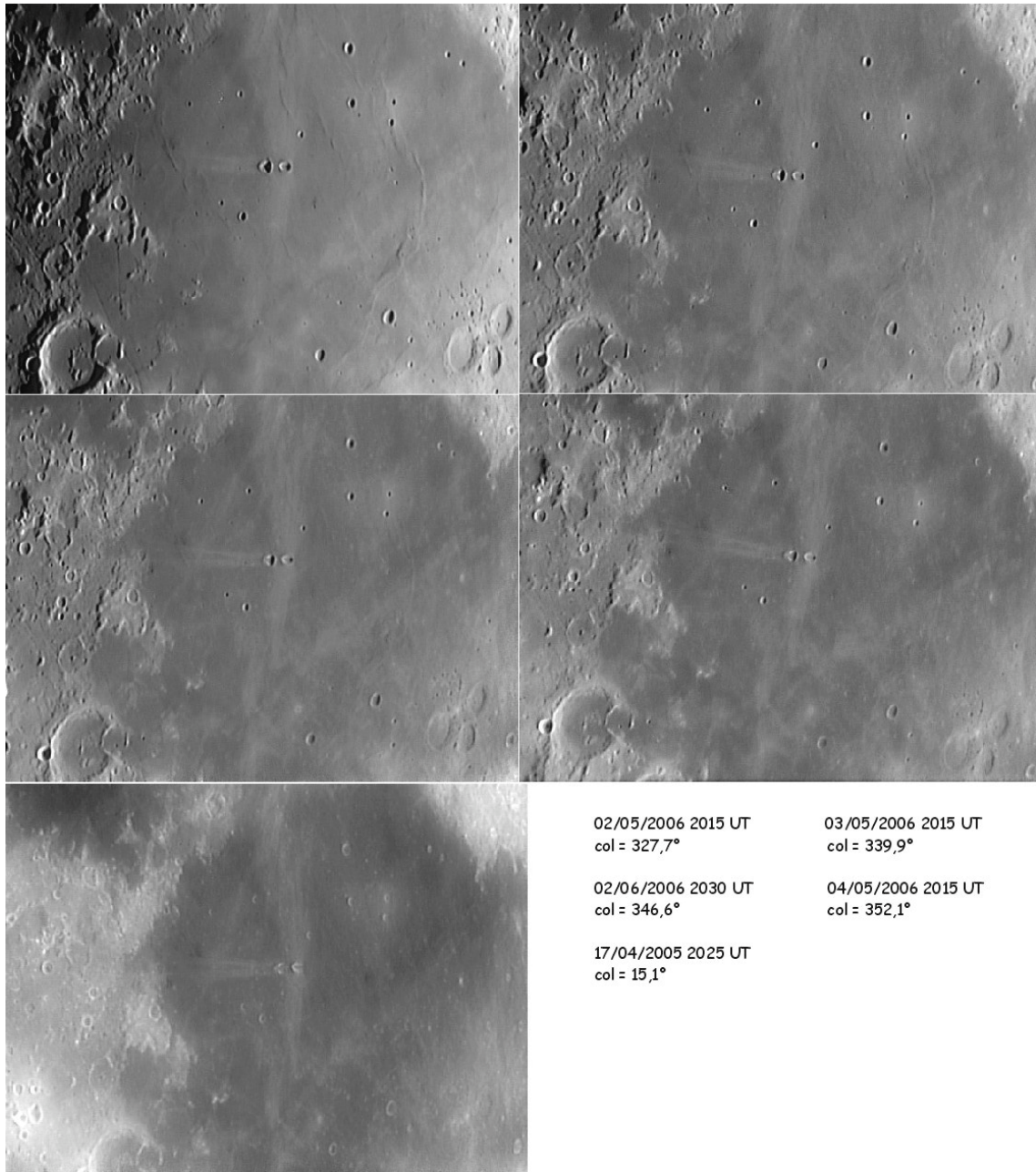col = 352,1°
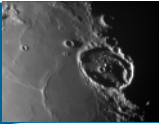
17/04/2005 2025 UT
col = 15,1°

Figure 7 Observations of sunrise over Messier and Messier A photographed with the 20 cm F15 refractor of Beisbroek Public Observatory. A webcam in prime focus was used. This sequence shows the comet tail type and butterfly-type of ejecta deposit of both craters during sunrise over Mare Fecunditatis.
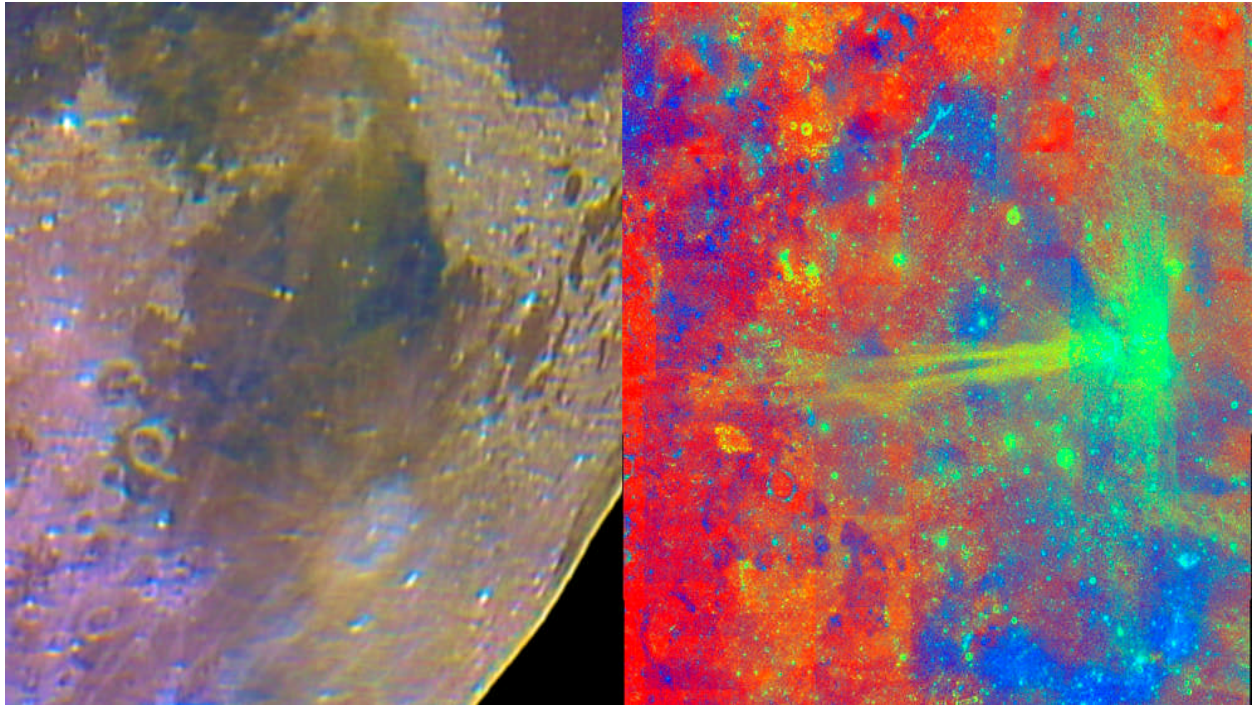
Figure 8 Enhanced colour image of Mare Fecunditatis and surroundings made with a 20 cm F6 Newton and webcam in prime focus on 15 October 2005 (left). The right hand side picture is a Clementine colour ratio image. The colour image is made with red being the ratio of 750 to 415 nm, green being the ratio of 750 to 950 nm and blue being the ratio of 415 to 750 nm.

photoelectric-photographic study of the normal albedo of the Moon. At full moon, when no shadows are visible from earth, the distribution of reflectivity appears to express actual variations in the composition or surface characteristics of the lunar surface materials. The diffuse reflectivity of the full moon is commonly expressed as normal albedo, the brightness of the lunar surface divided by the brightness of a Lambert surface when observer and light source are along the same normal vector. A Lambert surface is an ideal diffuse reflecting surface. It is non absorbing and uniformly bright from any viewing direction. Pohn and Wildey (1970) give a map of the earth-faced side of the Moon of the normal albedo (scale approximately 1/5000000 at the equator). Their map is used to construct a more detailed normal albedo map of the surroundings of Messier and Messier A. The map of Pohn and Wildey (1970) was used to calibrate the image of 04/05/2006 (see figure 7). Pixel brightness (grey values) of a number of points distributed over the image was plotted against normal albedo. Thereafter, a polynomial of second degree was fitted between these points. This polynomial gives a relation between pixel brightness and normal albedo over the range of pixel brightness of the calibration points. With this relation, the image was then recalculated. For the grey value of every pixel, the normal albedo is calculated. The result is given in figure 10. Normal albedo values in the interval 0.080 to 0.105 are given. Smaller or larger values were not used for the calibration and are thus also not given. Figure 11 gives the relation between pixel brightness and

normal albedo used to calibrate the image. This figure also gives the 50% confidence interval of the derived normal albedo values. This approach used here is very simple since for instance no corrections for variations in solar elevation and viewing angle are made. Utilising a different image or the same image processed in a different way would result in a different relation shown in figure 11 since pixel brightness would be different. The applied calibration procedure is strictly only valid for an incidence and an emission angle which are uniform across the field of view. However, the examined region appears to be sufficiently small for this approximative approach, since the normal albedo map (figure 11) and map of the 50% confidence interval (figure 11) does not show systematic large-scale variations across the surface of Mare Fecunditatis, which would be expected in the presence of major miscalibration. Figure 10 shows that the normal albedo of the Messier and Messier A rays is fairly high, around 0.100. From the study of Hawke et al. (2004), it is now known that although the ray material is of a basaltic composition, it is immature. Hence the high normal albedo. This is also the case for other geological young ejecta deposits in Mare Fecunditatis. The normal albedo of the rays decreases distally from the source crater. This is especially noticeable for the two rays west of Messier A. The mare itself has a normal albedo between 0.09 and 0.095. The lowest normal albedo is found in the northwest corner of the mare. These regions correspond with dark blue areas in the Clementine colour ratio image. The western part of the two Messier A

Figure 9 Enhanced colour image of Messier and Messier A using the 20 cm F15 reflector of Beisbroek Public Observatory (Belgium) and a webcam in prime focus. This is the same image (04 May 2006) as used in figure 7.
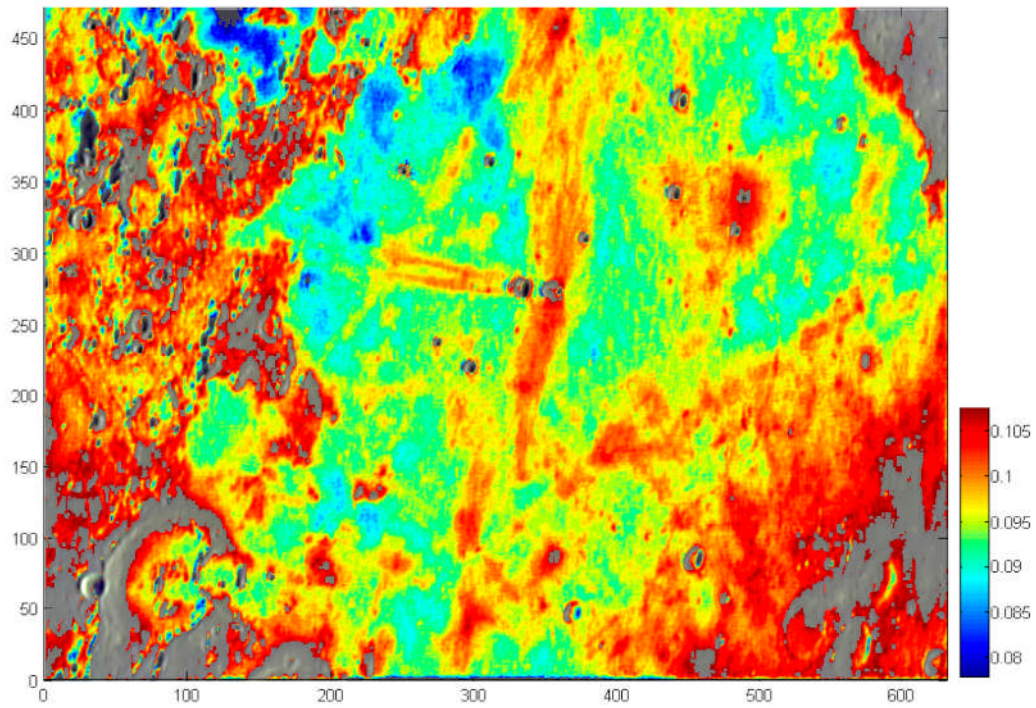
Figure 10 Normal albedo map based on the 04/05/2006 image. Values smaller then 0.080 are indicated in blue, values larger than 0.105 are indicated in red.
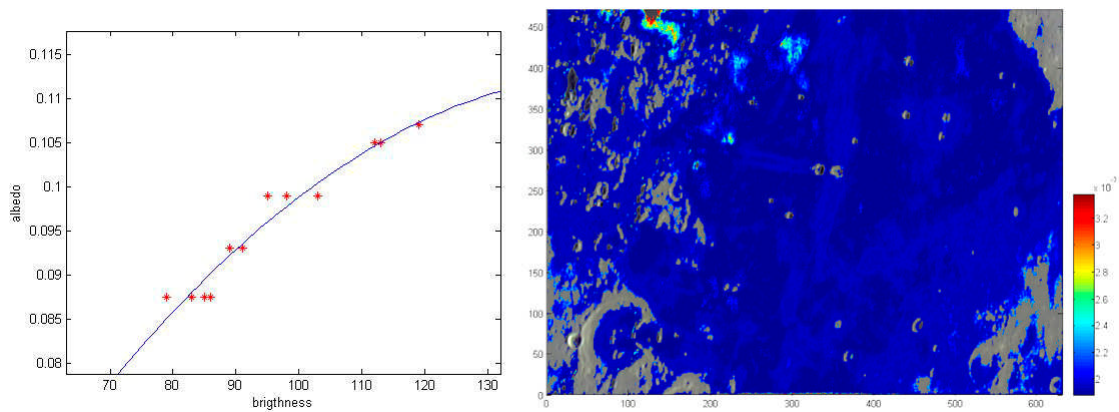

Figure 11 Pixel brightness (greyvalues) versus normal albedo (left) with the second order polynomial fitted through the data points. Right figure gives the 50% confidence interval of the derived normal albedo values.

rays are superposed on such blue low normal albedo region perhaps adding to the noticeable lesser brightness of the western part of these rays.

References

[1] Andre, C.G., Wolfe, R.W., Adler, I., 1979. Are early magnesium-rich basalts widespread on the Moon? In: *Proc. Lunar Planet. Sci. Conf. 10th*, 1739-1751.

[2] Dembowski, W.M., 2003. International Bright Lunar Rays Project: the Messier A system. *Selenology*, vol 22, no 4.

[3] Elston, D.P., 1974. Geologic map of the Colombo quadrangle of the Moon.

[4] Gault, D.E. and Wedekind, J.A., 1978. Experimental studies of oblique impact. *LPSCP 9*, v 3 p 3843-3875.

[5] Guest, J.E. and Greeley, R., 1977. *The geology on the Moon*. Wykeham Publications (London) LTD.

[6] Hawke, B.R., Blewet, D.T., Lucey, P.G., Smith, G.A., Bell III, J.F., Campbell, B.A. and Robinson, M.S. 2004. The origin of lunar crater rays. *Icarus*, 170, 1-16.

[7] Hill, H. 1991. A portfolio of lunar drawings.Cambridge University Press.

[8] Pickering, W.H. 1904. *The Moon.*

[9] Pieters, C.M. 1978. Mare basalt types on the front side of the moon, a summary of spectral reflectance data. LPSCP 9, 3, 285-2849.

[10] Pohn, H.A. and Wildy, R.L., 1970. A photoelectric-photographic study of the normal albedo of the Moon. *USGS Profesional Paper* 599-E.

[11] Rükl, A., 1996. *Atlas of the Moon*. Kalmbach Publishing Co.

[12] Sheenan, W.P. and Dobbins, T.A., 2001. *Epic Moon: A history of lunar exploration in the age of the telescope.* Willmann-Bell, Inc.

[13] Wanders, A.J.M., 1949. *Op ontdekking in het Maanland*. Uitgeverij Het Spectrum.

[14] Wilhelms, D. 1987. The geologic history of the Moon, USGS Prof. Paper 1348.

THE THIRD DIMENSION: CRATER DEPTHS FROM THE APOLLO ERA TO THE PRESENT

By Kurt Allen Fisher, member Salt Lake Astronomical Society

advances in consumer astrophotography and computing provide an opportunity for amateurs to make continuing contributions to lunar topography studies.

Abstract

A digitized table of 1,866 higher accuracy crater depths from the Apollo era associated with U.S. Geological Survey Gazetteer of Planetary Nomenclature (GPN) positions is provided in the supplementary materials. 86% of the craters in table have diameters less than 20km and 83% have depths of less than 2km. Existing catalogues of crater depths and feature heights have a 5 to 10% variation for craters with diameters larger than 10 km and up to 30% for craters less than 10 km.

Developments increasing the accuracy of techniques used to measure the height of lunar topography are reviewed from the Apollo era to the present, including lunar control point networks, digital elevation models from stereophotography and laser altimetry, Doppler radar interferometry, photoclinometry, and shadow measurements. Even with technological developments,

1. Introduction

"How big and how deep is that hole?" are common questions received by lunar observers from the general public. Yet answering that question with a reasonable degree of scientific certainty is more difficult than appears on initial inspection. Lunar topography is a statistical science. There is no absolute true height of Mons Piton or depth and diameter for Bessel H. There are statistical estimates for those values which have an inherent uncertainty.

A few standard references that are consulted for the depths of larger named lunar craters include Westfall's compilation of crater diameter and depth catalogues and Viscardy's Earth-based shadow measurements (Westfall 2000, Viscardy 1985). The GPN is another well-known standard reference for crater diameters which incorporates earlier work by Andersson and Whitaker. (USGS 2006b, Andersson and Whitaker 1982). Although Andersson and Whitaker (and the GPN) contain high-accuracy crater diameters, the catalogue rounds crater diameters to the nearest kilometer. The catalogue includes no crater depths or feature heights.

Table 1 – Measurements of the diameter and depth of Tycho and its central

Researcher	Diameter (km)	Depth (km)	Central peak height (km)
US Air Force, NASA and ACIC LAC 112 1967		4.46	1.56-2.19
Wood 1973			2.26
Pike 1976	85	4.6	
Andersson and	102		
Viscardy 1985	88	4.8	
Margot *et al.* 1999a	85	4.7	2.4

Table 2 - Crater diameter to depth relationships

Researcher	Applies to crater dia. km	N crater	Equation
Elachi et al. 1976	< 15km	16	Dp=0.2*Drc
Pike 1974	< 15km	171	Dp=0.196*(Drc^1.010)
Pike 1974	> 12 - < 275km	33	Dp=1.044*(Drc^0.301)

When the depth or diameter of archetypal features are compared between catalogues – such as the diameter of Tycho or the height of its central peak – variations of greater than 10% can be found between different sources (Table 1). Less well known are a series of high-accuracy crater depth and feature height data made during the Apollo era by Arthur, Pike and Elachi with respect to smaller satellite feature craters. (Arthur 1974, Elachi *et al.* 1976, Pike 1976, and Wood 1973). These researchers based their work in part on oblique stereophotography from the Lunar Orbiter missions of the 1960s and Apollo 15, 16 and 17 Command Modules. Thirty years later their work still represents some of the highest accuracy topography data available on the lunar nearside lunar surface: *Despite the fact that the Moon has been visited by six manned missions and a multitude of unmanned spacecraft, its surface is far from being completely explored. . . . [T]he best available set of spacecraft images globally covering the lunar surface, taken under low to moderate illumination angles and thus revealing the relief of the lunar surface, is still that obtained during the Lunar Orbiter programme in the mid-1960s.* [Lena 2006.] Part of higher accuracy Apollo era catalogues of Arthur, Elachi *et al.*, Pike and Wood have been associated here with standard GPN feature names. Those crater depth and diameter measurements, mostly for smaller satellite features, are digitized in the supplementary materials. While answering the questions "How big and how deep is that hole?", a review of Apollo era topography studies also tells an interesting story of a portion of that exploration's history. This historical review is intended as a continuation of Davis 1997 for the period 1996 through 2006.

2. Crater depth and diameter measurements during the Apollo Era

2.1. 1500 meter accuracy - Lunar Aeronautical Chart (LAC) measurements from Earth based telescopes. In 1960, D.W.G. Arthur, E. Moore, J.W. Tapscott and E.A. Whitaker (Gerard Kuiper ed.) published the *Photographic Lunar Atlas*, a compilation of lunar terrain photographs from the best telescopes in the world (St. Clair *et al* 1979). Companion volumes were published: the *Orthographic Atlas of the Moon* in 1961 and the *Rectified Lunar Atlas* in 1962 (Kuiper 1961, Whitaker, Kuiper and Hartmann 1963, St. Clair *et al* 1979). Rectification removes foreshortening and displays features on the lunar surface in their correct geometrical relationship. The Army Corps of Engineers' 1964 Topographic Lunar Map represented the first Apollo era attempt to create a nearside lunar elevation map - now commonly called digital elevation maps or "DEMs" - from which the relative altitudes of features could be ascertained (Army Map Service 1964).

The 1964 Topographic Lunar Map (TLM) has a vertical resolution of 1,000 meters based on a sphere of 1737.988 kilometers. All elevations were based on a low-nearside zero elevation point on the floor of Aristarchus which was measured to be about 7,000 meters below the floor of the Möstling A (Schimerman, U.S. Defense Mapping Agency 1973 at Sec. 4.1.7). Recent values for these elevations are 1735.96 kilometers for Aristarchus (ULCN 2005 Control point BA4127C) and 1737.465 (ULCN 2005 Control point 8) for Möstling A– a relative elevation difference of about 2 kilometers (Archinal *et al.* 2006b). The Topographic Lunar Map was developed from stereo-projection of plates taken at the Paris Observatory between 1896 and 1907 at different libration angles. No uncertainty statement concerning elevations is provided on the TLMs.

In the early 1960s, the Aeronautical Chart and Information Center of the U.S. Air Force published the Lunar Aeronautical Chart (LAC) series as navigational aids for the Apollo missions. St. Clair provides a retrospective of the U.S. Defense Mapping Agency (USDMA) LAC program and other USDMA Apollo charting efforts (St. Clair *et al* 1979).

The LAC charts were based in part on photocomparator measurements of Pic du Midi Observatory telescopic photographs of the Moon (Arthur 1974, p. 116). The stated uncertainty is printed on each chart. For example, LAC 112 for the Tycho region reads: "The probable error of the localized relative elevations is 100 meters in the vicinity of the center of the moon with the magnitude increasing to 300 meters at 70° from the center due to foreshortening."
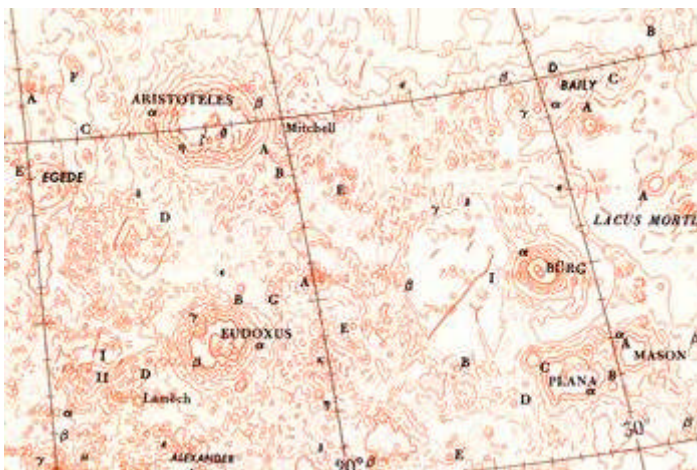

1 - Topographic Lunar Map (Excerpt for the region ...nding Aristoteles, Eudoxus ...ürg)

There is a systematic bias of up to 1500 meters present in the original LAC charts (C.A. Wood, 2006 personal communication). The systematic error in the LAC charts is traceable to the Pic du Midi Observatory negatives (Arthur 1974, p. 117). The elevation of lunar features can be stated in either relative or absolute terms. In a table of relative feature heights, for example the crater depth table in the supplementary materials, only provides information the relative distance between the mean rim crest of a crater and its mean floor. Absolute elevations are expressed with respect to a common base elevation and are more useful. For the Moon a typical base elevation is 1,739km. Charts based on absolute elevations are more useful. Absolute elevation charts provide not only the height of the central peak of crater Tycho relative to its floor, but also inform the users of whether the central peak of Tycho is in absolute terms higher or lower than the central peak of Arzachel.

To convert relative elevation data on a series of images or charts to absolute elevations, a series of control points – locations whose three dimensional positions are well-established – must be used to register each image or chart into a common coordinate system. The control point network used to align a series of images or charts into a common system also has its own uncertainty, separate from relative elevation measurements on an individual chart or image.

Charts in the LAC series are a hybrid of relative and absolute elevation methods. Most of the measurements on the chart series are relative, *e.g.* the central peak of Tycho on LAC 112 is 1.56km above the crater floor in one direction and 2.2km above the floor in another direction. Control points with absolute elevations are plotted separately, *e.g.* the floor of the satellite feature Kaiser C (S36.3, E9.7, dia. 12.45km) shown on LAC 112 is listed at an absolute elevation at a lunar radius of 1,739.1km; the rim to floor depth is 1.35km, and the rim to surrounding plane height is 0.54m. A later higher accuracy depth measurement, listed in the supplementary table, shows Kasier C's depth at 2.52km. In the ULCN 1994, discussed below, Kasier C is listed with an absolute elevation at a lunar radius of 1,737.2 km.

The Aeronautical Chart and Information Center (ACIC) Selenodetic System of 1965 (revised 1969) provided a network of 150 control points that supported the absolute elevations listed on the LAC series (St. Clair *et al* 1979). The ACIC of 1965 was prepared from Earth-based telescope observations and had a horizontal accuracy of 500 to 2000 meters (St. Clair *et al* 1979).

LAC topographic crater measurements and control points are illustrated in the following excerpt from LAC 26 for the crater Eudoxus. A control point in the floor of crater Eudoxus D at elevation-radius 1,739.4 km is highlighted by the red box.

Figure 2 - Lunar Aeronautical Chart 26 (Excerpt for the region surrounding Eudoxus)

During the early 1960s, the United States Geologic Survey (USGS) under the direction of Eugene Shoemaker prepared the Geologic Atlas of the Moon, a 13-color geologic chart series that parallels the LAC series (Cherrington 1984 at 45).

2.2. 100 meter vertical accuracy - the Lunar Orbiter IV image measurements

By 1965, D.W.G. Arthur concluded that unexplained abnormally large errors in earth based telescope measurements could not give useful data on the diameters and relative depths of smaller craters (Arthur 1974, p. 117).

1966 through 1967 brought the first systematic remote satellite imaging of the Moon by the Lunar Orbiter I-V series. Arthur undertook measurement of smaller craters based on Lunar Orbiter IV images to a two-significant digit precision. During 1969 through 1973, Charles Wood joined the Lunar and Planetary Laboratory, University of Arizona, working under D.W.G. Arthur, and supervised the higher precision measurement of the diameter and relative depth of about 7,000 nearside craters using Lunar Orbiter IV images (Wood 1974, unpublished, Wood 2004).

Arthur published approximately 1,900 of Wood's measurements including crater size, crater depth and Arthur crater class (Arthur 1974). Arthur described prosecution of the work as follows:

The work was performed by student assistants under the immediate supervision of Charles A. Wood. I set out the general guide lines of the work and formulated the special mathematics required for the reduction. Occasional visits were sufficient to exercise general supervision and to deal with special problems. . . . [Arthur found that] [t]he smaller lunar craters are indeed smaller than indicated by the ACIC [LAC] determinations and those of Baldwin [Arthur 1974, p. 117].

With respect to approximately 1,900 craters that are a subset of Wood's 7,000 plus nearside measurements, Arthur noted that his 1974 catalogue was restricted to those craters that have higher confidence measurements:The catalog of this paper is much briefer [than Wood's full catalogue], is restricted to those craters which were included in the measures, and is quite differently arranged. The two catalogs, however, contain the same depth results, except where I have suppressed heights relating to large irregular objects. Note that the measures were restricted to those craters in which the lower end of the shadow (the tip) fell close to the center of the interior of the crater [Arthur (1974), p. 118].

Arthur stated measurement uncertainty for the reduced catalogue at +- 100 meters for large complex craters and +- 25 to 50 meters for smaller simple craters (Arthur 1974, p. 121). Although the original Wood catalogue covers the entire nearside, in the smaller higher confidence catalogue, Arthur limited crater depth data to a spherical square bounded the north-south 45° and east-west 45° selenographic meridians (Arthur 1974, p. 120) as shown in Figure 3.

1610 diameter and relative depth measurements from Arthur's catalogue are digitized in the supplementary material table. The remaining crater depths either could not be associated with GPN names or did not meet the inclusion criterion discussed in the Appendix.

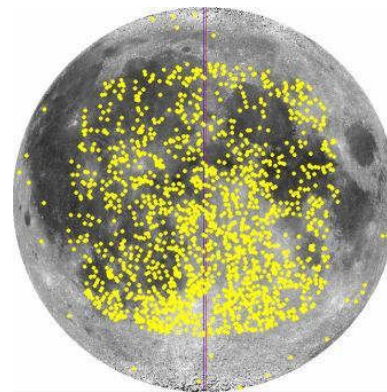Arthur also developed a new method for reducing feature heights and depths from shadows.

Figure 3 - Distribution of Arthur 1974 crater depths presented in the supplemental materials. Image - LTVT

In the classical reduction method derived from Earth based observations, the geometry of Earth, Sun and Moon relationship are determined from a lunar ephemeris, the angular size of the hypotenuse shadow is determined using a reticule, microfilament or lunar photograph and the linear height of the feature is estimated (Chervel and Legrand 1994, Kopal 1962, MacDonald 1931). Jamieson's DOS lunar reduction tool software – which is based on MacDonald's classical mathematical algorithm for shadow measurement - historically has been used lessen the burden of reduction of Earth-based shadow measurements (Davis 1997, Jamieson 1997, Jamieson 1993).

In Arthur's reduction method for Lunar Orbiter images, an initial guess of the linear size on the Moon of the hypotenuse shadow is made (for example, from a rough chart take-off), the order of computation is reversed and an estimate of the photographic linear size of the hypotenuse shadow and the height of the feature are made. Itineration is used to minimize the root mean square error of the estimate of the size of hypotenuse shadow on the photographic image (Arthur 1974, p. 118-120). This also yields a final estimate of the height or depth of the feature.

Wood also estimated the heights of approximately 37 central peaks of craters (Wood 1973).

2.3. 100 meter vertical accuracy - Lunar Topographic Orthophotomap (LTO) series

High-resolution photography from the Command Module of the last three Apollo missions - Apollos 15, 16 and 17 - launched another phase in lunar cartography.

The images for the nearside roughly correspond to a "V" shaped band running between N20° and S20° selenographic latitudes shown in Figure 4.

Stereographic photomaps were prepared by the U.S. Defense Mapping Agency from the Apollo images - the NASA Lunar Topographic Orthophotomap (LTO) series - with an unprecedented depth accuracy stated by Schimerman: *"The evaluated horizontal and vertical accuracy of subject series at 90% probability generally ranges from 160-500 meters and 30-115 meters respectively . . . [Schimerman, U.S. Defense Mapping Agency 1973.]"*

A sample excerpt for a 100-meter accuracy LTO map for the Apollo 15 - Mt. Hadley landing site is shown in Figure 5.
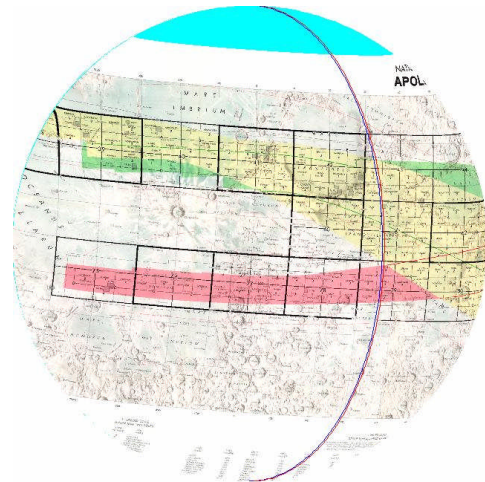

Figure 4 - **NASA 1980. Lunar Topographic Orthophotomap (LTO) Series Apollo Photo and Map Index Map** **fitted to lunar globe. Image - LTVT**
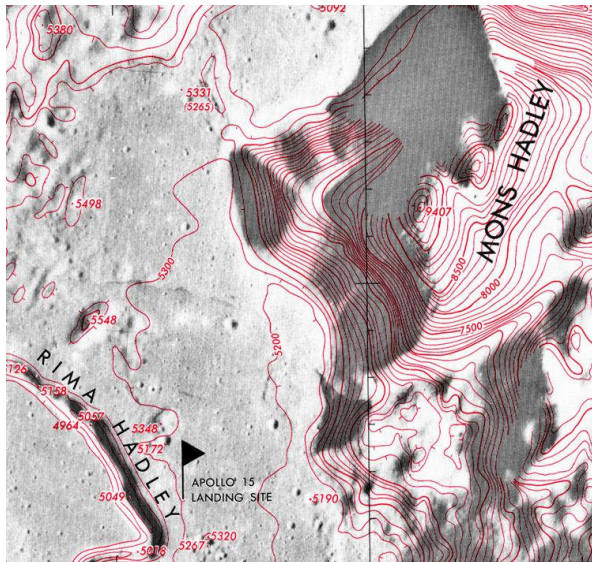
Figure 5 - [U.S. Defense Mapping Agency 1975. Map LTO-41B4](#) **(Excerpt)**

Individual maps in the series contain additional accuracy statements. [Map LTO-41B4](#) states a 90% accuracy of 176 horizontal meters and a vertical accuracy of +-41 meters. The LTO series are available by internet download from the [Lunar and Planetary Institute](#).

Although highly accurate, the LTO series covers less than 20% of the Moon's near and farside surface ([Archinal *et al.* 2005](#)).

2.4.   20-50 meter accuracy - Lunar Topophotomap (LTP) series

Micromaps of specific lunar features from the Apollo stereograms - the [NASA Lunar Topophotomap (TPM) series](#) - where prepared by the U.S. Defense Mapping Agency with 20 meter contour lines.

The uncertainty for each map is printed in its legend. Typical is map [LTP 41B4S1(50)](#) for the Apollo 15 Mt. Hadley landing site which states a horizontal accuracy of 61 meters and a vertical accuracy of +-20 meters.

The LTO and TPM series represent a major advancement over the LAC series in lunar topographic charting. All elevations on the LTO and TPM series are absolute with respect to common base elevation of 1,730km. For example, on map [LTO-41B4](#), crater Hadley C is shown as having floor at an elevation of 4,230 meters, a rim at 5,500 meters and the surrounding plain at 5,100 meters. This implies a crater depth of 1,270 meters. The table in the supplementary materials lists Hadley C with a depth of 1,160 meters.

The Apollo 15 Control System provided a network of 5,629 control points based on Apollo 17 LIDAR data and Apollo 15, 16 and 17 stereophotographs ([St. Clair *et al* 1979](#), [Archinal *et al.* 2005](#)).

2.5.   Pike's crater depth measurements from the LTO and LTP series

Pike used a combination of measurements from Arthur, lunar topographic orthomaps, Lunar IV imagery and Apollo 15 through 17 panoramic picture cameras to measure numerous dimensions for 484 craters and other features on the near side Moon ([Pike 1976](#)).

The table presented in the supplementary materials extracts 212 of Pike's crater measurements for diameter and depth that easily could be associated with GPN listed features. The remaining measurements in Pike's catalogue are for unnamed craters, non-crater features, craters with no corresponding GPN entry or craters that did not meet the inclusion criterion described in the Appendix.

Pike's catalogue also indicates whether a crater has a central peak, but does not record the height of the central peak. Figure 6 shows the distribution of part of Pike's and Elachi *et al*'s catalogues (discussed below) on the nearside. Compare to Figure 4, above.
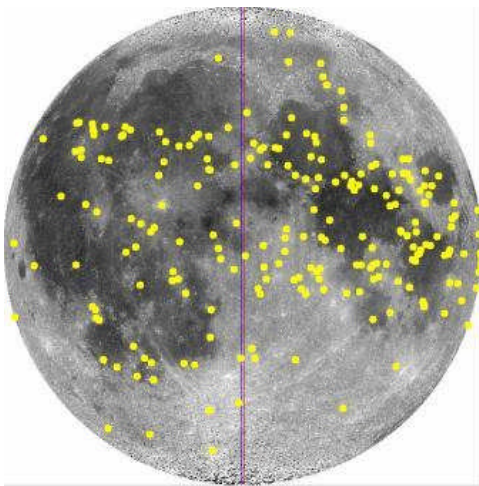

Figure 6 – Distribution of features digitized from Pike 1976 and Elachi *et al.* 1976. Image - LTVT

2.6. 25 meter accuracy - Apollo 17 radar altimeter and Elachi *et al.* depth measurements

Elachi *et al.* reported the results of a radar altimeter that was attached to the Apollo 17 Command Module - the Apollo Lunar Sounder Experiment (ALSE) (Elachi *et al*. 1976). (The lead researcher, Dr. Charles Elachi, is presently a director of the Jet Propulsion Laboratory and a leader on the Cassini Titan radar team (JPL 2006).) The ALSE provided a continuous 30 kilometer wide swath of altimeter readings, including profiles for large maria like Crisium, Tranquilitatis and Serenitatis. Elachi *et al.* also reported high precision 25 meter accuracy crater diameters and depths for 16 craters. Ten of these 16 craters could be easily matched to the GPN and seven are included in the supplementary material table. Smaller crater measurements cover features in Arthur 1974.

2.7. Relationships between crater dimensions

2.7.1. Crater depth to crater diameter relationships

Among the features measured by Pike, included:

Rim diameter - average rim-crest to rim-crest diameter;

Depth - vertical distance from the rim diameter elevation to the crater's central low point;

Floor diameter - diameter of the floor to terraced or slumped walls;

Rim flank - horizontal distance from rim crest to elevation of the level of surrounding plain;

Rim height - vertical distance between rim crest to elevation of the level of surrounding plain;

Apparent diameter - the diameter of the crater at elevation of the level of surrounding plain; and,

Apparent depth - vertical distance from the apparent diameter elevation to the crater's central low point (Pike 1976, *id*. at Fig. 1, Pike 1977).

In *The Lunar Sourcebook*, Heiken *et al*. summarizes empirical relationships found from the Apollo era data (Heiken *et al.* 1991 at Table 4.1). Such empirical mathematical relationships are all in the form of

y = a * Drc^b

where a and b are coefficients and "Drc" is the rim to rim diameter of the crater.

Pike found empirical relationships between crater depth and diameter based on 170 small craters less than 15km in diameter (Pike 1974). Elachi *et al.* also plotted small crater depths to their diameters, finding that for his small sample of craters less than 30 kilometers in diameter, the ratio of the crater depth was constant at 0.2 (Elachi *et al.* 1976, *id*. at Fig. 2).

For large craters, Pike also found an empirical relationship of rim-to-rim crest to depth of about Drc^0.3.

Pike did further follow-up work on the crater diameter to depth relationships based on apparent crater volumes as opposed to rim-to-rim crest diameters (Pike 1977). These diameter to depth relationships are summarized in the table 2 and figure 8. A plot of the ratios of 1,905 crater depths to diameters – an expanded set of craters from the list in the supplemental materials– is shown in Figure 7 and illustrates Elachi *et al*.'s small crater depth to diameter ratio of 0.2*Drc.

In Figure 7, the trend line is fitted to 11 of 16 of Elachi *et al*.'s craters.
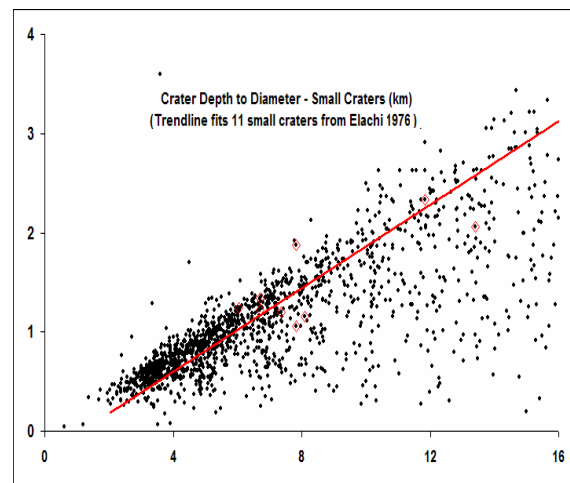

Figure 7 - Small crater (<15km) depth to diameter relationship

Pike's large crater depth to diameter relationship is illustrated in Figure 8 by crater diameter for 1,905 nearside craters. To improve graphic clarity, Figure 8 plots the reciprocal of Pike's large crater relationship – the ratio of the crater depth to diameter to crater diameter.
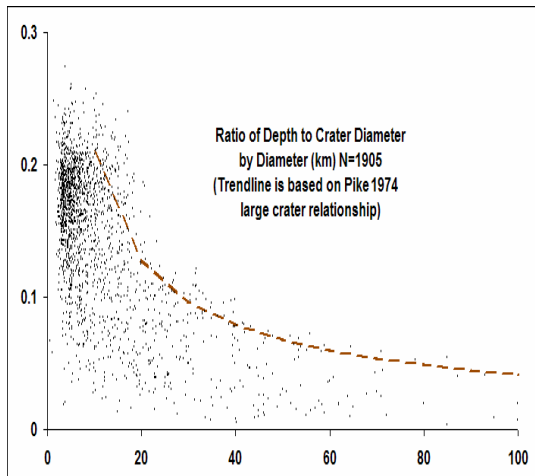

Ratio of Depth to Crater Diameter by Diameter (km) N=1905 (Trendline is based on Pike 1974 large crater relationship)

Figure 8 - Large crater (>12 km) depth to diameter relationship

Wood and Andersson examined 2,589 fresh Copernican nearside craters in more detail (Wood and Andersson 1978).

They defined morphology classes for this group of young craters into statistical archetypes represented by Albategnius C, Biot, Sosigenes, Triesnecker, and Tycho.

Wood and Andersson better defined equations statistically relating the diameters of craters in each morphological subtype to their depths and central peak heights.

They reconciled differences between crater diameter to depth relationships found in their larger crater sample and in Pike's previous work based on differences between subpopulations of highland and mare craters.

2.7.2 Central peak height to crater diameter relationships

Hale and Head measured the characteristics of crater diameter, rim crest height and central peak height for 90 nearside and 85 farside craters from the LTO map series for craters larger than 17 km in diameter (Hale and Head 1979). This was part of a continuing series of studies following up on Wood 1973.

They proposed equations to relate rim crest crater diameters and the crater floor width to the height of the crater's central peak.

Hale and Head did not publish a catalogue of craters and central peak heights on which they based their conclusions.

Hale and Grieve performed a similar analysis based on digitized LTO maps and the volumes, not diameters, of craters (Hale and Grieve 1982).

The empirical relationship between crater rim-to-rim diameter and central peak height is summarized in the following table 3 and graph, shown in Fig. 9.
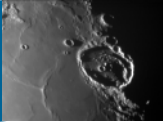
Table 3 - Crater to central peak height relationships

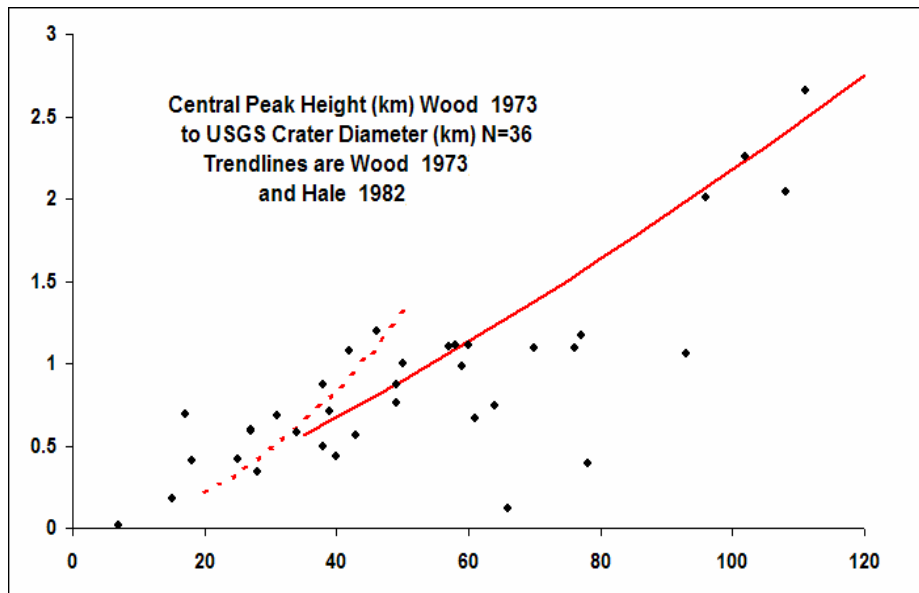| Researcher	Applies to crater dia. km	Equation
Wood 1973	> 35km	Hcp=0.006*(Drc^1.28)
Hale and Grieve 1982	> 17km - < 51km	Hcp=0.000589*(Drc^1.969)

Figure 9 - Diameter to Central Peak Height Relationships after Hale and Grieve 1982 and Wood 1973

As noted above, Wood and Andersson better defined diameter to central peak height relationships for young fresh craters ([Wood and Andersson 1978](#)).

That Pike did not record central peak heights and that Hale and Head did not publish a catalogue of central peak heights creates an amateur research opportunity ([Pike 1976](#), [Hale and Head 1979](#)). Pike identified about 80 craters as having a central peak that are on LTO 100-meter accuracy maps, but for which there is no currently published 100-meter accuracy central peak height measurements. A 100-meter accuracy central peak height measurement might be recovered for these craters from the LTO maps.

2.8. NASA Catalogue of Lunar Nomenclature (NCLN) 1982

After Wood's departure from the Lunar & Planetary Institute in 1973, Wood's work was continued on farside craters by Leif Andersson under the direction of Ewen A. Whitaker. The combined Wood-Arthur and Andersson-Whitaker catalogues were published in 1982 by [Andersson and Whitaker 1982](#). [Andersson and Whitaker 1982](#) is often referred to by its common title - the NASA Catalogue of Lunar Nomenclature (NCLN). The NCLN contained a reduced data set: only crater diameters are reported, not depths. Depths are rounded to whole kilometers.

The [NCLN](#) contains no statement of uncertainty for crater diameters.

The [NCLN](#) also sought to reconcile IAU recognized features with NASA feature assignments. Leif Andersson, who passed away shortly before the publication of the NCLN, was honored post-humously by assignment of his name to C. Andersson, a 13 kilometer diameter crater at S49.7, W95.3. Jonathan McDowell digitized the NCLN in 2004 ([McDowell 2004](#)).

1995 saw the first publication of the GPN by Batson and Russell (Batson and Russell 1995). The current online version of the GPN is accessible over the internet ([USGS 2006b](#)).

3. Measurements based on the Clementine era

3.1. 900-1000 meter accuracy depths - Clementine Digital Elevation Models (DEMs)

1994 saw the Clementine multi-spectral lunar imaging mission. Clementine took multi-spectral images of the lunar surface, took photographic stereograms, and using a laser altimeter and ranging instrument (LIDAR) located absolute elevations for approximately every 512 square kilometers of the lunar surface with spacing varying between 20 and 100 kilometers depending on terrain ([USGS 2002](#)). Clementine collected 72,548 LIDAR elevation points between 79° south and 81° north ([USGS 2002](#)). Clementine LIDAR points have a vertical accuracy of 130 meters ([Archinal *et al* 2005](#)). Figure 10 shows a plot of Clementine LIDAR altimeter points from about 45 north to the north polar limit.
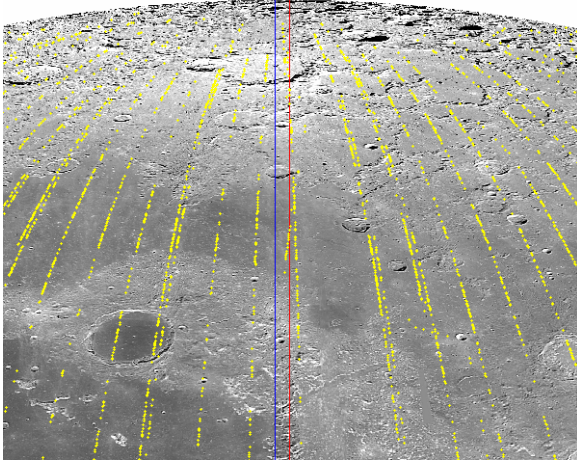
Figure 10 - Clementine LIDAR points. Image – LTVT

LIDAR technology can measure the distance between two points with a high degree of precision and reliability between a known and an unknown point, but the vertical accuracy of Clementine LIDAR points is dependent on the accuracy of the orbital model that provides a reference position of the satellite with respect to the center of the lunar body.

The Clementine spacecraft was a moving orbiter of the Moon, a body whose gravitational field varies greatly (Konopliv *et al.* 1998). Because of variations in the Moon's gravitational fields, the orbits of lunar spacecraft generally are unstable (Bell 2006).

In 1994, Zuber, Smith and Lemoine *et al* produced the first accurate global topographic model of the Moon using Clementine LIDAR data, named the Goddard Lunar Topography Model-1 (GLTM-1) (Zuber, Smith and Lemoine *et al* 1994). In 1997, the accuracy of GLTM was improved (GLTM-2) (Smith *et al.* 1997, Lemoine *et al.* 1997). The GLTM-2 model had a vertical resolution of 100 meters and a horizontal resolution of 2.5º. An improved GLTM-2B data set with a horizontal resolution of 0.25º or 900 meters is available by internet distribution (NASA and Washington Univ. 2006a). The following figure plots the GLMT-2B topographic model. Light areas are higher in elevation; darks areas are lower. The GLTM-2B model is valid to north/south 78º lunar latitudes.
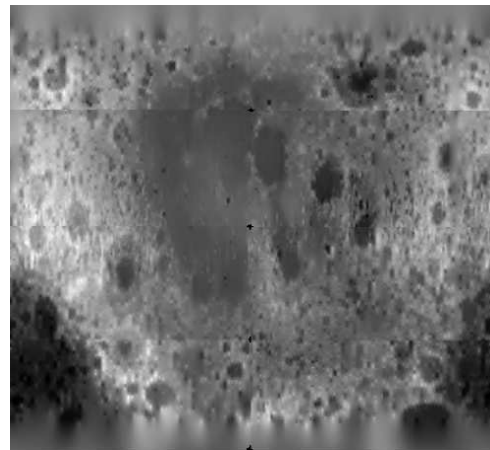

Figure 11 - Plot of GLTM-2B data from NASA and Washington Univ. 2006a. Image - author

These digital elevation models have a low-topographic resolution with respect to individual crater features as compared to earlier stereo-photo-comparator elevation maps, including the 1964 Topographic Lunar Map or the mid-1970s Lunar Topographic Orthophotomap (LTO) series. Although the LIDAR altimeter points have a much higher level of accuracy at widely-spaced measuring points, once combined with stereograms into a digital elevation model, the accuracy of the final digital elevation model is reduced. The reduction in horizontal resolution of 100-150 meters in Clementine visual band stereograms to 1 kilometer resolution bins in a final lunar digital elevation map also was dictated by the need to conserve computing resources: "Images are matched for every other pixel in the overlap region in each stereo pair - matching every pixel would unfortunately quadruple the expected processing time of four months. The sampling spacing of matched points, every 2x2 pixels, although smaller than a final 1 km DEM pixel size, can provide ~50-100 height measurements per DEM pixel for a single stereo pair since the UVVIS image pixel size is 100-150 m/pixel. The DEM pixel size of 1 km, although lower in resolution than the original UVVIS images, is useful for two purposes: 1) it compensates for most gross navigation errors in camera pointing, and 2) it allows the averaging of many height points contained within each 1x1 km pixel, thus improving the topographic signal to noise ratio over that of a single stereo matched point" [Cook *et al.* 2000].

Using a combination of Clementine LIDAR elevation data and stereograms, Rosiek *et al.* produced a digital elevation map of the north and south lunar poles between 64º north and south latitudes and the north and south lunar poles with a vertical accuracy of approximately 180 meters (Rosiek *et al.* 2001).

Rosiek *et al.* merged a Clementine LIDAR digital elevation map, Clementine stereophotos, and pre-existing shaded relief maps into an updated full-Moon LIDAR topography map with a 1km horizontal resolution (Rosiek *et al.* 2002, USGS 2002). The vertical error of the LIDAR topography map is 180 meters at the north pole and 164 meters at the south pole. This dataset forms one core of the USGS Map-A-Planet online application and its option to plot a "Clementine LIDAR topography" map (USGS 2006d, USGS 2006e). The 2002 Rosiek *et al.* map also is available in a petal leaf format (USGS 2002).

Cook *et al.* prepared a whole Moon digital elevation model based on a 5km and a 1km horizontal resolution in order to better reduce noise in vertical measurements. The resulting models had a +-300 meter vertical uncertainty in 5km horizontal model and a +-100 meter vertical uncertainty in the 1km model. (Cook *et al.* 2002).

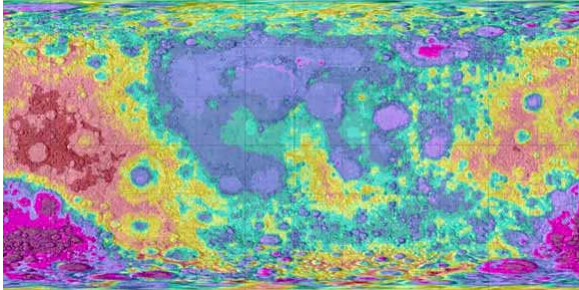Figure 12 shows a Clementine digital elevation map in Mercator projection of the whole Moon (Archinal *et al* 2006c).

Figure 12 - Full Moon Topography Mercator Projection from Archinal *et al* 2006c. Image - USGS

The Rosiek *et al.* 2002 digital elevation map was combined with an air-brush terrain map of the lunar surface with 900 meter per pixel resolution in USGS Map Series 1-2769 (USGS 2003). The I-2769 datasets form another core of the U.S.G.S. Map-A-Planet online application familiar to many amateur lunar observers. USGS Series 1-2769 is the map that displays as shaded-terrain relief in USGS Map-A-Planet renderings of the lunar surface.

Rosiek continued refinement of the 2002 model, correcting for errors in the 1994 CLCN, and in 2006 issued a revised whole Moon topography model – the ULCN 2005 Topographic Model (Archinal *et al* 2006a, Archinal *et al* 2006b). On 18 January, 2007, the U.S.G.S. internet distributed the ULCN 2005 topographic DEM (Archinal *et al* 2006c). The ULCN 2005 DEM can be displayed using USGS using private vendor software licensed by the USGS for free public redistribution (Archinal *et al* 2006c, USGS 2006f). The freeware also allows to user to register images to the DEM, to overlay DEM contours onto a user image, and to graph line-of-sight elevation profiles.

The Figure 13 (next page) from the ULCN 2005 topographic model shows a DEM and contour plot for the same region surrounding Aristoteles, Eudoxus and Bürg as is depicted from the 1964 Topographic Lunar Map, above at Figure 1. The 200 meter contours in this DEM excerpt are relative to a baseline lunar radius of 1,737.4 kilometers.

Although of low-resolution compared even to the 1964 TLM, the ULCN 2005 topographic DEM can provide useful information with respect to large craters. The resolution of the DEM is too low to capture a sharp crater rim. The DEM does provide information on the relative height of larger crater floors to surrounding plains as shown in the Figures 14.

See Figure 13 (next page) with respect to the profile sight-line for Aristoteles and Rükl Charts 3, 4 and 11 for Plato profile sight-line.

In 2007, Rosiek *et al* announced the computation of preliminary revised 1 kilometer and 5 kilometer resolution DEMs based on the new ULCN 2005 model (Rosiek *et al* 2007). The revision updates Rosiek *et al* 's 2002 DEM and covers 35% of the Moon's surface. 66% of the DEM tiles have a vertical accuracy between 300 and 500 meters; 33% have a vertical accuracy between 500 and 1000 meters.

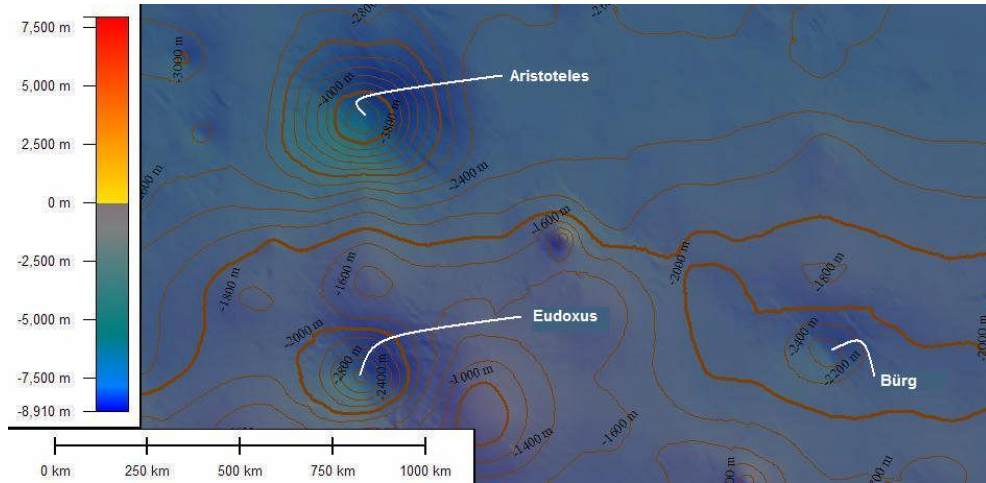**Figure 13 - ULCN 2005 topographic DEM (Excerpt for the region surrounding Aristoteles, Eudoxus and Bürg, image covers approx. 12° lunar latitude by 20° longitude). Image – USGS Dlgv32 Pro**
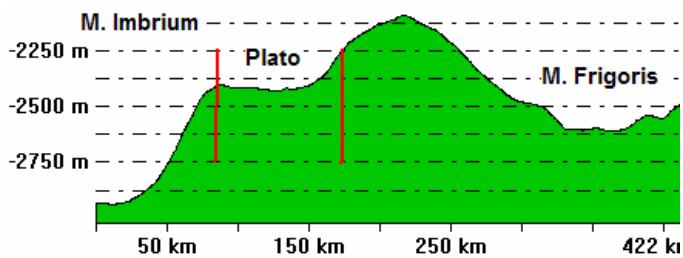

Figure 14 - Profiles of Aristoteles (top) and of Plato (bottom) from M. Imbrium to M. Frigoris at W 10° longitude generated from the ULCN 2005 topographic DEM (Archinal *et al* 2006c). Image – USGS Dlgv32 Pro

3.2.137-219 meter accuracy depths – Clementine Control Point Networks

Interplanetary body control point networks, like their terrestrial counterpart, provide for the location of local features on a body's surface where the body's fundamental points are obscured by the local horizon (Schimerman, U.S. Defense Mapping Agency 1973 at Sec. 3.0). The local control points provide an intermediary reference between the feature's position and fundamental points. In addition for computing feature positions, control networks can be used register lunar images to maps of the Moon's surface. For the Moon, fundamental points are usually taken as the center of the Moon's spheroid and/or the center of the floor of satellite feature Möstling A at S3.2, W5.2 lunar latitude and longitude.

In 1994 and prefatory to analysis of Clementine mission images, Davies *et al*. prepared an updated control point network of 1478 points, 1286 of which are on the nearside, commonly known as the Unified Lunar Control Network (ULCN 1994) (Davies *et al.* 1994a, USGS 2006c).

ULCN 1994 is based on improved processing of data from the Apollo 15 control system, on imagery from the Mariner 10 and Galileo missions, and on Earth-based photography (USGS 2006c).

ULCN points have a horizontal accuracy of 100 meters to 3km and vertical accuracy of a few kilometers (Archinal *et al.* 2005, USGS 2006c). ULCN 1994 control points are generally located on the floors of satellite feature craters. ULCN 1994 is included as a data file in Mosher's and Bondo's Lunar Terminator Visualization Tool, discussed below, or is available by internet download from the USGS (Mosher and Bondo 2006, Davies *et al.* 1994b).

In 1997 as part of processing Clementine images into mosaics, Merton Davies and Tim Colvin created the Clementine Lunar Control Network (CLCN) – a set of 271,634 control points (USGS 2006c). The CLCN was used to register over 40,000 Clementine images into the digital elevation models discussed above. The accuracy of the CLCN was called into question and in August 2006, Archinal *et al.* issued a corrected set of 272,931 3-D coordinates – the Unified Lunar Control Network 2005 (ULCN 2005) (Archinal *et al.* 2006b).

The ULCN 2005 has a mean vertical uncertainty of 137 meters, with a first standard deviation error of 219 meters (Archinal *et al* 2006c at 2). The mean horizontal position accuracy is 335 meters with a maximum three standard deviation error of 5.1 kilometers (Archinal *et al* 2006c at 3). The control points have a density of one point per 46 km^2, or one point every 6.8 kilometers.

In 2007, Archinal *et al* announced the completion of the ULCN 2005 Control Network and Lunar Topographic Model (Archinal *et al* 2007). Planned improvements to the control network and model have been placed on hold due to United States federal budget cuts.

3.3. 100-325 meter accuracy crater diameters - Clementine base map images

Clementine visual images were taken at too high a sun angle in order to be useful for shadow depth or height measurements (Lena 2006). But Clementine 750nm base map images can be used for the study of horizontal crater diameters.

The Clementine 750nm base map images, also available from USGS Map-A-Planet, have a horizontal resolution between 100 to 325 meters and typically cover about 40 square kilometers (USGS 2006e). The USGS Map-A-Planet Clementine images display in a rectified format and can be used to measure crater diameters with common desktop paint utilities.

The USGS Map-A-Planet applet displays the resolution of the image at the bottom of screen in pixels per kilometer.
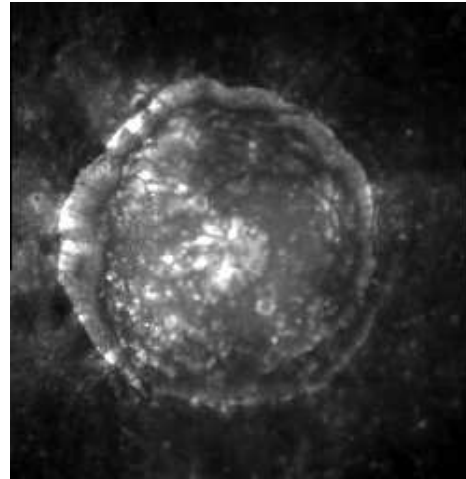
Figure 15 - C. Plinius (dia. 41.2 km) at 237 meters per pixel resolution. Image - USGS Map-A-Planet

Clementine base map images are also available from NASA Planetary Data Services as collections CL-3001 through CL-3015 (NASA 2006a).

3.4. 20-100 meter accuracy crater diameters - Clementine HiRes polar image map

Two other Clementine image series are available at higher resolutions, but finding and using the images related to specific features requires more effort.

The images in these collections do not display in a rectified format, making reduction of crater diameters from the images complicated.
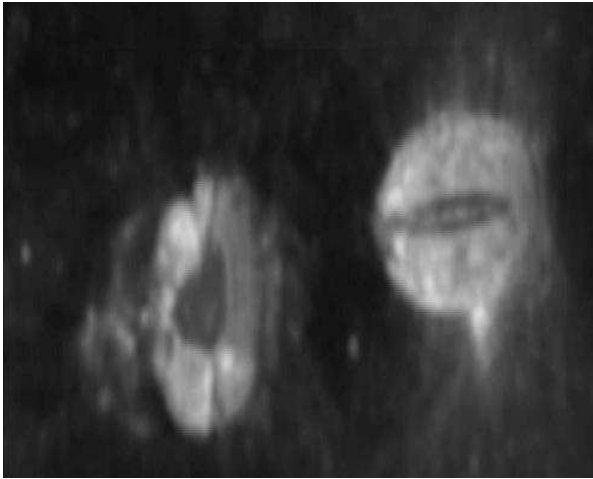
Figure 16 – Messier A (dia. 13.25 km) and Messier (dia. 11.63 km) from CL-4013, Image UI03S045, at 100 meters per pixel. Image - NASA PDS

The PDS Clementine CL-4001 through CL-4078 image series provides a slightly higher precision of 100 meter horizontal resolution over the CL-3000 series (NASA 2006b). The PDS Clementine Data Node also provides internet distribution of the Clementine HiRes polar image map with a 20-30 meter horizontal resolution as collections CL-6001 through CL-6022 (NASA 2006c). These images are not rectified. Clementine 750nm base map, HiRes and HiRes polar images are stored at the NASA Washington Univ. (St. Louis) Planetary Data Systems (PDS) Clementine Data Node (NASA-Washington Univ. 2006b). The PDS Clementine Data Node provides a browser image viewing interface for some collections.

NASA-JPL also provides a desktop viewer compatible with Clementine PDS stored images for either Windows, Apple/Macintosh or UNIX operating systems (NASA and JPL 2006).

3.5. Digital elevation models from Clementine data vs. Apollo era stereophotograph measurements

Because Clementine digital elevation models aggregate vertical elevation data in 1,000 meter horizontal bins, they do not provide a significantly improved level of vertical accuracy (180 meters by Rosiek *et al.* 2001 and 100 meters by Cook *et al.* 2002) as compared to the 61 horizontal meter by 20 vertical meter accuracy achieved by the Apollo era Lunar Topophotomap series or the 160-500 horizontal meter and 30-115 vertical meter accuracy of the Apollo Lunar Topographic Orthophotomap series.

Digital elevation models on a 1,000 meter horizontal resolution also have limitations with respect to small craters depths for features located on irregular terrain. At a 1km resolution, the odds of having elevation points on a rim crest or crater floor become small. Conversely, with respect to larger craters, digital elevation models make craters more amenable to volumetric fitting, similar to that explored by Hale and Grieve in the 1980s based on digitization of the LTO map series (Hale and Grieve 1982).

In this respect, Clementine era digital elevation models have a lower vertical resolution than the Apollo era data discussed above. Conversely, the Clementine digital elevation models have coverage over the entire Moon with all measurements being expressed with respect to a 1737.4 kilometer idealized surface. Control point systems like ULCN 1994 and ULCN 2005 have a vertical uncertainty greater than the Apollo era data discussed here.

4. Measurements from the Earth-based radar interferometry era (1997-2006)- 20 meter vertical accuracy and 150 meter horizontal accuracy

Earth-based radar mapping of the Moon began in the post-World War II era using surplus military antennae.

Thompson produced a whole nearside Doppler radar map of the Moon to a resolution of 1 kilometer using the Haystack and Arecibo radio observatories (Thompson 1979).

Stacey continued and expanded this work using the Aricebo observatory by developing new Doppler radar analysis techniques that could image to a 20 meter resolution (Stacy et al. 1997).

Since the mid-1990s, four researchers, B.A. Campbell, D.B. Campbell, N.J.S. Stacy and J.L. Margot, have pioneered the use of radar interferometry to prepare high resolution maps of lunar craters (Stacy et al. 1997, Margot et al. 2000 and Campbell et al. 2004).

Their efforts have been principally focused on mapping possible ice deposits at the lunar poles (Stacy et al. 1997, Margot et al. 2000 and Campbell et al. 2006). In the search for lunar ice deposits, Margot and B.A. Campbell each illustrate how the technique is usually used to achieve 400 meter resolution near the lunar limb, but can be pushed to a 150 meter horizontal and a 20 meter vertical resolution (Margot et al. 2000 and B.A. Campbell et al. 2005).

Margot et al. prepared a detailed topographic map of the crater Tycho with a horizontal resolution of 200 meters and a vertical resolution of 20 meters using Earth-based radar interferometry (Margot et al. 1999a).

Margot et al. found that Tycho's central peak rises 2,400 meters above the mean crater floor and that the crater's depth was 4,700 m between mean rim and mean floor. Compare with Apollo era estimates in Table 1. A radar map image of Tycho can be found in Figures 5 and 6 of Margot et al. 2000.

Margot et al. also prepared the north and south lunar pole radar interferometer maps of the north and south lunar poles above north-south latitudes 87.5° to a horizontal resolution of 150 meters and a vertical resolution of 50 meters (Margot et al. 1999b).

B.A. Campbell *et al.* produced a 300 meter horizontal resolution radar map of Posidonius (Campbell *et al.* 2003). A 400 meter horizontal resolution radar maps of the lunar south pole and for the lunar nearside have been produced (Campbell *et al.* 2004, Campbell *et al.* 2005).

B.A. Campbell *et al.* prepared a 20-meter horizontal resolution image of the Cobra's Head on the Aristarchus Plateau and a digital elevation model of Reiner Gamma formation (Campbell, Carter and Campbell *et al* 2006).

D.B. Campbell *et al.* achieved 20 meter vertical resolution in mapping C. Shoemaker at the lunar south pole (Campbell and Carter 2006). In October, 2006, based in part on this increased resolution, D.B. Campbell *et al.* concluded that it was unlikely that there were ice deposits at the south lunar pole (Campbell *et al.* 2006).

Like shadow measurements, the accuracy of Doppler radar is not uniform across the nearside. Shadow measurements decrease in accuracy closer to the lunar limb. Doppler radar is more accurate (300-400 horizontal meters) closer to the lunar limbs but decreases to 900 meters for features near the central annulus of constant radar signal return. (Margot *et al.* 2000, Campbell *et al.* 2005).

Although Doppler radar studies are currently focused on lunar ice at the poles, the north and south lunar pole digital elevation models with 20 meter vertical resolution could be used to prepare enhanced accuracy crater depth, diameter and volume catalogues. As of this date they have not be used for that purpose. Using Earth-based Doppler radar, a 20 meter vertical resolution digital elevation map of the entire nearside appears technologically feasible.

5. Local feature DEMs from Shape-from-Shading (SFS) photoclinometry

As shown in Figure 14 above, whole-Moon DEMs based on orbiter stereophotography and LIDAR measurements have low detail resolution even for large craters. An alternative method for rendering localized DEMs is photoclinometry based on "shape from shading" (SFS). The basic concept underlying SFS photoclinometry is that a lunar surface reflects light in proportion to Sun's altitude in the lunar horizon system of the feature to be studied.

5.1 Computationally complex SFS algorithms after Hapke and Kirk

If a surface is a uniform diffuse-light-scattering surface – it is a Lambertarian surface. Few lunar surfaces reflect light in a uniform manner due to variations in surface composition. Hapke provides a computationally complex method for quantifying the reflectance of lunar surfaces (Hapke 1993).

Hapke's methods are incorporated by Kirk into a software package called *Integrated Software for Imagers and Spectrometers* (ISIS) (USGS 2007, Kirk, Barrett and Soderblom 2003). ISIS currently is used by researchers on Mars orbiter missions to convert Mars images to DEMs. ISIS will be used on future lunar missions, described below, for the same purpose.

5.2 Reduced computational SFS algorithms after Wöhler, Hafezi and Lena *et al*

Wöhler and Hafezi and Lena, Pau and Phillips *et al* described a computationally reduced algorithm for constructing local feature DEMs that measures lunar feature elevations to accuracy similar to more intensive Kirk-Hapke SFS algorithms (Wöhler and Hafezi 2005, Lena, Pau and Phillips *et al* 2006). A reduced level of computation is achieved, in part, by assuming that the lunar surface to be measured is a uniform diffuse-light-scattering Lambertarian surface (Wöhler and Hafezi 2005).

Many classes of lunar features do not meet this basic criteria and are excluded as suitable candidates for SFS-photoclinometry. Such classes of features have albedo variations related to the changes in surface mineral composition.

Examples include radial banded craters like Bessarion, dark mantle pyroclastic deposits near Rima Bode, the cryptomare in Schickard, magnetic swirls like Reiner Gamma, dark halo craters like Copernicus H, dark-rayed craters like Dionysius, and, in high-altitude lighting, bright-rayed craters like Tycho. Not all bright-rayed craters are excluded. As discussed below, some bright-rayed craters reflect uniform-diffuse light in the visible band under low-angle solar illumination.

Figure 17 – Local feature DEM for part of the East slope of Copernicus (radius ~ 46.5 km). Image - Wöhler and Hafezi 2005. Reprinted from Pattern Recognition, 38(7), Wöhler and Hafezi, General Framework for Three-Dimensional Surface Reconstruction, pp. 965-983, © 2005, with permission from Elsevier.
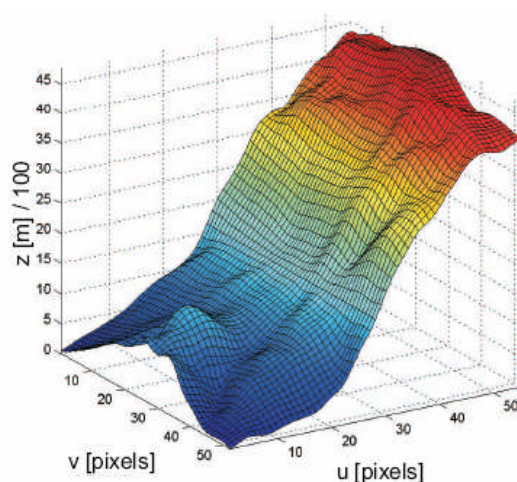
SFS-photoclinometry works best in low Sun illumination – less than 20-30º. Low illumination angles imply the SFS works best on features with a height above surrounding plain of one kilometer or less. Under low illumination, terrain on the shadow side of a feature still will reflect light. Information on terrain gradient from reflectance will not be lost in dark-deep shadows, as occurs for tall mountains and ridge systems on the edge of basins. Where a lunar feature does meet the basic criteria of uniform diffuse reflection, the SFS-photoclinometry algorithm described by Wöhler and Hafezi and Lena, Pau and Phillips *et al* can be applied. The Wöhler and Hafezi algorithm structurally is forward-fitting (Kirk, Barrett and Soderblom 2003 at 3-4). Conceptually, the SFS algorithm is simple:

A computational DEM matrix is initialized with zero elevation heights;

A seed albedo of a flat or nearly flat surface within the user's image is found based slope analysis determined from classical shadow measurements;

The height and albedo of each pixel in the DEM matrix is estimated from pixel's current estimated slope;

The residual error between each pixel's computed albedo in the computational DEM matrix and the user's image is estimated.

The height of each pixel in the DEM matrix is updated based on the pixel's residual error;

and the DEM matrix is recomputed until the residual error of each pixel is minimized (Lena, Pau and Phillips *et al* 2006, Wöhler and Hafezi 2005).

The Geologic Lunar Research Group (GLR Group) has applied this SFS method to a variety of lunar features, discussed below.

5.2.1 20%+ height accuracy – SFS-photoclinometry of craters and miscellaneous features using the Wöhler and Hafezi algorithm

Examples of Lambertian surfaces on the Moon that can meet the basic photoclinometry criteria of uniform diffuse surface reflectance include wrinkle ridges on mares, straight faults on mares and some craters. The Lambertian reflectance law is a good approximation to the true reflectance behaviour for regions near the centre of the lunar disk, viewed under oblique illumination and perpendicular view. For large phase angles above 110-120 degrees, the Lambertian approximation even remains valid for more oblique viewing angles.

Wöhler and Hafezi demonstrated SFS-photoclinometry on these classes of features (Wöhler and Hafezi 2005).

Examples of their local feature DEMs for a wrinkle ridge, straight fault and part of a large crater are shown in Figure 17 to Figure 19.
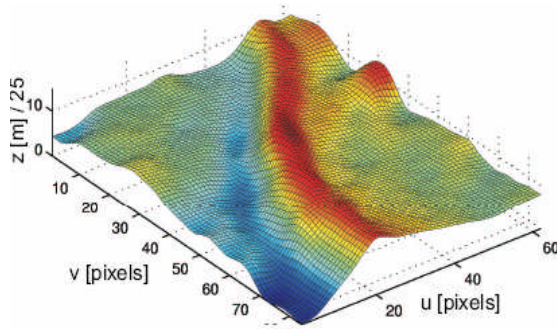
Figure 18 - Local feature DEM for a mare wrinkle ridge south-west of crater Aristarchus. Image - Wöhler and Hafezi 2005. Reprinted from Pattern Recognition, 38(7), Wöhler and Hafezi, General Framework for Three-Dimensional Surface Reconstruction, pp. 965-983, © 2005, with permission from Elsevier.

Figure 19 - Local feature DEM for the north end of Rupes Recta (~ 10 km by 10 km) Image - Wöhler and Hafezi 2005. Reprinted from Pattern Recognition, 38 (7), Wöhler and Hafezi, General Framework for Three-Dimensional Surface Reconstruction, pp. 965-983, © 2005, with permission from Elsevier.

Resolution in these local feature DEMs is much greater than whole-Moon DEM resolution shown in Figure 13 above. The modern depth estimate for Copernicus is 3,800 meters (Pike 1976).

Per Geologic Lunar Research Group (GLR Group) members Wöhler, Lena and Lazzarotti, the typical standard error for height measurements obtained through SFS-photoclinometry is 20% (Wöhler, Lena and Lazzarotti *et al* 2006). Lighting anomalies can produce height artifacts, *e.g.* – the crater in the upper left-hand corner of Figure 19 (Wöhler and Hafezi 2005).

Because many wrinkle ridges, straight faults and craters may have albedo variations confounded by changing surface mineral composition, SFS-photoclinometry should applied to such features with caution.

Application of multiple measuring techniques to a feature (shadow measurements and light profiles) and false color ratio imagery can minimize spurious measurements of heights and corroborate the photoclinometry result (*e.g.* Lena, Wöhler and Bregante *et al* 2006, Wöhler and Hafezi 2005).

5.2. Less than 100 meters – SFS-photoclinometry of lunar domes

Domes are one of the best lunar features that meet the basic SFS-photoclinometry criteria of uniform diffuse reflectance. That lunar domes reflect diffuse light uniformly is known to many amateurs who have conducted a futile search for these features in high-altitude lighted Clementine images. Lunar domes generally are indistinguishable from their surroundings in Clementine 750nm base map images precisely because they reflect light uniformly and at the same intensity as the surface materials that surround an individual dome. This characteristic of high-altitude Clementine photographs of lunar domes makes those images unsuitable for stereophotography, but conversely shows that lunar domes are good candidates for SFS-photoclinometry (Wöhler, Lena and Lazzarotti *et al* 2006).

Figure 20 – Six lunar domes north of C. Hortensius, ~ 6 to 12 km in dia, contained within the boundaries of this Clementine 750nm base map image are almost invisible. Hortensius' dia. is 14 km. Image - USGS Map-A-Planet

GLR Group members Kapral and Garfinkle published a catalogue of approximately 2,500 verified and unverified domes and other miscellaneous features (Kapral and Garfinkle 2005). The Kapral-Garfinkle catalogue is a compilation of domes compiled from approximately 25 journal and other sources, including the Journal of the Assoc. of Lunar and Planetary Observers. Of those entries, approximately 750 involve verified and unverified domes (as opposed to miscellaneous features) and 186 verified and unverified domes have associated height measurements. The distribution of those 186 domes is plotted in Figure 21. The distribution of 751 verified and unverified domes with known diameters do not differ significantly from Figure 21 and are not plotted separately here. A digitized catalogue is provided by the GLR Group (Kapral and Garfinkle 2005). This catalogue is also plotted by the GLR Group on a copy of the LAC charts (Shaw 2006).

Figure 21 - Distribution of 186 verified and unverified domes with listed heights per Kapral and Garfinkle 2005. Image - LTVT

Figure 22 - Distribution of heights of 130 verified domes per Kapral and Garfinkle 2005

The morphology of domes also is favorable to application of SFS photoclinometry. Lunar domes tend to be about one kilometer in height and at most 20 kilometers in diameter (Hiesinger and Head 2006 at 42). At low solar illumination, lunar domes do not cast dark, deep shadows on the shadow-side of a feature. The distribution of heights of verified lunar domes from Kapral and Garfinkle are shown in Figure 22. Ninety-five percent of the domes have heights less than 1.2 kilometer; sixty-six percent have heights less than 400 meters.

The GLR Group's Wöhler *et al* described a SFS-photoclinometry technique that uses dome albedo to measure the height of lunar domes down to below a 100 meter level of precision (Wöhler, Lena and Lazzarotti *et al* 2006). The stated precision is 10 percent for dome heights and 5 percent for dome diameters (Wöhler, Lena and Lazzarotti *et al* 2006).

Traditional shadow measurements of lunar dome heights yield "slope and height values consistent with those obtained by the [SFS] image-based 3D reconstruction (Wöhler, Lena and Lazzarotti *et al* 2006).

5.3   20%+ height accuracy – SFS-photoclinometry of lunar domes using the minimal SFS algorithms of Carlotto 1996

Evans described a SFS-photoclinometry technique, using simple Excel spreadsheets, to measure lunar dome heights after the computationally minimal technique of Carlotto (Evans 2006a, Carlotto 1996). Evans' Excel spreadsheet can be obtained through the *Selenology Today* website (Evans 2006b). In Carlotto's method, SFS computation is reduced to a minimum by using astrophotography software to rotate a lunar dome so the apparent solar azimuth incidence is 270º. Evans demonstrated that Carlotto's method produces elevation models that have an accuracy of about 9% of the elevations obtained in the GLR Group lunar dome studies (10%) discussed above. This implies about a 20% height accuracy for lunar domes. In addition to the basic SFS criteria of uniform reflectance, Carlotto notes that his method is limited to scenes illuminated by Sun altitudes of less than 20-30º. Evans recommends that the method only be used for features between 30º N/S lunar latitude due to the effect of foreshortening. The end-result of this SFS process are pixel scaled elevation maps similar to Figure 18, above, or a wireframe model similar to Evans' rendering of the 12.2 kilometer diameter Cauchy Omega dome. The Lunar-Lambert model behaves very similar to the simple Lambert model near the centre of the lunar disk but strongly deviates from the Lambert model near the limb.

6.   Modern amateur Earth-based astrophotography and shadow measurements

How accurate can amateurs measure crater depths and feature heights from the Earth using modern tools? Has amateur astrophotography progressed to the point in the last three years, where reasonably accurate height and depth shadow measurements from lunar photographs? Is their accuracy sufficient to compete with traditional Earth based micrometer measuring? Can they provide useful topographical data for specific features that supplements digital elevation models prepared from lunar orbiters?

The major components of error in making feature height or depth measurements by the classical shadow method include:

Accurate ephemeris;

Accuracy in determining feature coordinates;

Topographic slope variations;

Atmospheric seeing;

Computational error; and,
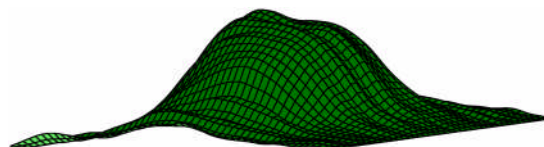
Technique in measuring shadow length (Davis 1997).

Figure 23 – A DEM wireframe rendering of Cauchy Omega. Image – Author from Evans 2006b data.

6.1. 10% height – Traditional amateur shadow measurements with microfilament meters

Amateur Bill Davis describes how he tested the accuracy of his use of a microfilament to measure the height of features on the Moon (Davis 1998). Davis called the ALPO's Dr. John Westfall. In the context of that work, Westfall suggested using the Lunar Topographic Orthophotomaps as a practice baseline. From 119 micrometer measurements, Davis found he estimated heights to within a 10% accuracy of the LTO map value for Mt. Harbinger and 18 other lunar mountains. Davis commented that the best measurements were made with a solar angle between 3 and 6 degrees.

Davis simulated shadow measurements for a 1,500 meter central peak and found that a 1 degree negative slope of a surrounding mare results in about a 23% over estimation of height; a 1 degree positive slope results in about a 16% under estimation of height (Davis 1997).

With respect to positive relief dome heights, Lena, Pau and Phillips *et al* suggest compensating for this confounding factor by estimating feature height from the difference between a morning and evening elevation measurement (Lena, Pau and Phillips *et al* 2006).

6.2. Lucky Imaging astrophotography combined with shadow measuring and light curve profiles

Recently, advanced amateurs like Paolo Lazzarotti regularly make lunar images with linear resolutions down to 0.11-0.22 arcsecs per pixel that correspond to sub-kilometer linear distances (*see* Wöhler *et al* 2007 at p. 76). For a lunar feature at N0, E0 when the Moon is at 384,440 kilometers distance, 0.11 arcsecs corresponds to about 200 meters.

There are competing parameters that affect the resolution of shadows in modern astrophotographs – the moving terminator versus repeated imaging over time.

The shadow cast by a lunar feature moves. At low oblique sun angles, the shadow cast by feature will be longer than 200 meters even though the feature is less than 200 meters in height or depth.

But at the equator, the terminator moves across the lunar disk at about 510 meters a minute. At 45 degrees north latitude, it moves at about 360 meters a minute.

Modern high-resolution amateur astrophotographs usually are acquired over time using the technique of "Lucky imaging" (Law, MacKay and Baldwin 2006, Tubbs 2004).

The astrophotographer (1) takes many images over several minutes, (2) selects images with the best point-spread function during a moment of atmospheric calm within a larger interval of atmospheric turbulence, (3) registers the image by cross-correlation, (4) averages the correlated images, and (5) applies filtering techniques such as convolution to the averaged image. The characterization of the technique as "lucky imaging" comes from the probability associated with taking an image during a moment of atmospheric quiet within a given interval of general atmospheric turbulence. During the first step of the lucky imaging process, the feature shadow moves between taking of individual images. Averaging images results in a fuzzy position of the shadow during the imaging session.

Jim Mosher and Henrik Bondo implemented a modern graphical user interface for the manipulation of and feature plotting on user lunar photographs – the Lunar Terminator Visualization Tool (LTVT) (Mosher and Bondo 2006). LTVT includes a shadow measuring tool. In order to model the accurate position of the lunar terminator and to determine the lunar azimuth and altitude of the Sun at a lunar coordinate, LTVT downloads high accuracy Jet Propulsion Laboratory (JPL) lunar ephemeris files. To assist in the accurate determination of lunar coordinates, LTVT includes a feature for registering a user lunar image to either 1994 or 2005 ULCN points. The shadow measuring tool does not follow the classical mathematical algorithm of MacDonald.

The accuracy of measurements made using LTVT's measuring tool has not been fully tested. LTVT is still in the post-beta revision, development and refinement stage. Initial anecdotal testing indicates that a crater depth accuracy between 5-10% compared to LTO map depths can be achieved with careful technique, including checking image alignment to 1994 ULCN control points (Wood 2006, Mosher, personal communication).

Another useful feature of LTVT, unrelated to shadow measurements but also worth noting, is its ability to easily rectify user lunar images.

Wöhler *et al.* described a topographic study of Rupes Bürg that applies shadow measuring to advanced modern lunar astrophotographs (Wöhler *et al.* 2007). Wöhler *et al.* estimated the height of Rupes Bürg at approximately 400 meters. Wöhler *et al.* also demonstrated how light profile curve tools, a feature of many common astrophotography software packages, can be used to characterize the topographic profile of lunar ridges.

There is no uncertainty statement for height measurements in Wöhler et al. 2007.

Davis's technique of using test measurements based on features on LTO and LTP maps in order to establish an accuracy baseline suggests a method by which amateurs can quantify the reliability of any technique that they use.

7. The Future – Geologic DEMs, SMART-1, SELENE and LRO

Calibrating multispectral imaging from the Clementine and Lunar Prospector missions with the spectrographic response of Apollo and Luna mission soil return samples has expanded and changed our understanding of global lunar surface geology (Hiesinger and Head 2006 at 8, 64-65).

The next logical step in the evolution of topographic DEM information and new geologic insights from multispectral remote sensing is the combination of the two data sets into a new geologic atlas of the Moon – updating the thirty-year old Apollo era atlas mentioned above (USGS, NASA and US Airforce ACIC 197_). In 2006, the USGS announced the first results of a pilot project funded by NASA to prepare a new geologic lunar map series on a 1:2,500,000 scale based on updated Clementine multispectral image analysis (Gaddis *et al* 2006). Gaddis *et al* includes a preliminary draft of the first quadrangle map produced by the pilot project for the Copernicus area.

New SMART-1 imaging has not been released for public access, as of this paper. Koschny *et al* discussed the distribution of SMART-1 images on the lunar globe (Koschny *et al* 2007).

Rosiek *et al.* have experimented using overlapping Lunar Orbiter, Apollo 15 and Clementine images of the Apollo 15 Mt. Hadley landing site to automatically generate digital elevation maps with the precision equal to the TPM series (Rosiek *et al.* 2006).

With respect to the SELENE mission to be launched in the summer of 2007, Honda *et al* described initial tests of stereographic mapping software designed to convert stereophotographs into digital topographic models (Honda *et al* 2007). SELENE's terrain mapping camera has a horizontal resolution of 10 meters/pixel. Software tests on simulated lunar surfaces where able to build DEMs with a vertical accuracy 5 to 25 meters for one standard error. Software tests on a Apollo 15 stereophotograph created a DEM that could resolve craters more than 100 meters in diameter and a rille about 1 kilometer in width. Yokota *et al* also demonstrated SELENE kilometer scale DEM software for the production of orthotopographic terrain maps, again using Apollo era stereophotographs as test data (Yokota *et al* 2007).

A SELENE mission goal is to prepare a new high accuracy global DEM based on low-altitude orbit stereophotographs. The mission intends to fill-in 80% of the lunar surface not covered the Apollo era stereophoto LTO maps (Honda *et al* 2007).

The Lunar Reconnaissance Orbiter (LRO) is scheduled to fly in October 2008. Chin *et al* describes the LRO's topographic-mapping related instruments, including a laser altimeter, an imaging camera and side-looking synthetic aperture radar. Data from these instruments will support new global topographic mapping and detailed mapping of cold traps at the lunar poles with between 15 to 100 meter horizontal resolution (Chin *et al* 2007).

8. Conclusion

This retrospective on the gathering of higher accuracy lunar crater and feature depth, height and diameter measurements represents one of many of the high-points of the Apollo era explorations. It represented a great-leap forward in our understanding of lunar topography. That effort continued through the Clementine era and subsequent Earth-based radar interferometry and will continue in future orbiter imaging missions.

There is a cautionary lesson-learned in this history. Some measurements from the Apollo era have been lost where catalogues were not preserved by publishing for later historical use.

Hopefully, the future will chart a path towards preserving raw measurements and preventing the loss of hard won lunar data while continuing the USGS-NASA practice of open internet distribution. At the 57th Annual International Astronautical Congress, NASA Chief Administrator Griffin asked that "lunar science data should be openly shared among the science community, just as we do with other planetary science data [Griffin 2006, p. 11]." Griffin suggested the collective sharing and standardized formatting of all data from upcoming lunar missions (Ellison 2006). In 2006, NASA announced a partnering initiative with the online search engine Google.com to distribute 3-D lunar surface renderings (NASA 2006d).

For amateurs concerned that pursuit of lunar topographic studies with amateur tools has been deprecated by digital elevation maps generated from orbiter missions, modern lunar astrophotography appears to have a level of precision sufficient to justify follow-up topographic study of individual terrain features. The foregoing review provides an overview of professional studies and resources, so the amateur can avoid duplicative effort, or use existing professional data as a baseline against which to practice technique and/or corroborate their depth-height measurements.

The Appendix describes the method by which a table of higher accuracy crater depth and central peak heights measurements from the Apollo era was developed and matched with the USGS GPN.

The table of digitized Apollo era crater depths is distributed electronically as supplemental material in the following formats (link):

Pdf

Html

Csv

The Appendix in Westfall's *Atlas of the Lunar Terminator* remains the best general amateur source for the depths of larger named crater depths (Westfall 2000).

References

Andersson, L.E. and Whitaker, E.A. 1982. *NASA Catalogue of Lunar Nomenclature (NCLN)*. NASA Reference Publication 1097. Archinal, B. A., Rosiek, M. R., Kirk, R. L. and Redding, B. L. 2005. Unified Lunar Topographic Model. *Space Resources Roundtable VII: LEAG Conference on Lunar Exploration*, Abstract No. 2060.

Archinal, B.A., Rosiek, M.R., Kirk, R.L. and Redding, B.L. 2006a. Completion of the Unified Lunar Control Network 2005 and Topographic Model. *37th Annual Lunar and Planetary Science Conference, 2006*. Abstract No. 2310.

Archinal, B. A., Rosiek, M. R., Kirk, R. L. and Redding, B. L. 2006b. A Clementine Derived Control Network and Topographic Model - The Unified Lunar Control Network 2005. *Progress in Planetary Exploration Missions, 26th meeting of the IAU, Joint Discussion 10, 21-22 August 2006, Prague, Czech Republic*. JD10, #26 (Abstract).

Archinal, B.A., Rosiek, M.R., Kirk, L.K., and Redding, B.L. 2006c. The Unified Lunar Control Network 2005. U.S. Geological Survey Open-File Report 2006-1367 (Ver. 1.0). URL: http:// pubs.usgs.gov/of/2006/1367/, (last date accessed 3 Feb. 2007) (See data file ULCN2005_LPOLY.zip for model)

Archinal, B. A., Rosiek, M. R., Kirk, R. L. , Hare, T. L. and Redding, B. L. 2007. Final Completion of the Unified Lunar Control Network 2005 and Lunar Topographic Model. *38th Annual Lunar and Planetary Science Conference, March 12-16, 2007, League City, Texas,* Abstract No. 1904. URL: http://www.lpi.usra.edu/meetings/lpsc2007/pdf/1904.pdf (last date accessed 7 Feb. 2007)

Army Map Service, Corps of Engineers. 1964 (2d). Topographic Lunar Map (West-half and East-half maps). URL: http://www.lpi.usra.edu/resources/mapcatalog/LTM/, (last date accessed: 2/3/2007).

Arthur, D. W. G. 1974. Lunar crater depths from Orbiter IV long-focus photographs. *Icarus*. 23:116-133.

Batson, Raymond M. & Russell, Joel F. 1995. *Gazetteer of Planetary Nomenclature*. U.S. Geological Survey Bulletin 2129. Washington: U.S. Government Printing Office.

Bell, T. 2006. Bizarre Lunar Orbits. (NASA Press Release). URL: http://science.nasa.gov/ headlines/y2006/06nov_loworbit.htm, (last date accessed: 7 January 2007)

Campbell, B. A., Campbell, D. B. and Nolan, M. 2003. New High-Resolution 70-cm Wavelength Radar Images of the Moon. *34th Annual Lunar and Planetary Science Conference, March 17-21, 2003, League City, Texas.* Abstract No.1700.

Campbell, B. A., Campbell, D. B., Hawke, B. R. and Lucey, P. G. 2004. Radar Properties of Lunar Basin Deposits. *35th Lunar and Planetary Science Conference, March 15-19, 2004, League City, Texas.* Abstract No. 1659.

Campbell, B. A., Campbell, D. B. and Chandler, J. 2005. New 70-cm Radar Mapping of the Moon. *36th Annual Lunar and Planetary Science Conference, March 14-18, 2005, in League City, Texas.* Abstract No.1385.

Campbell, B. A., Carter, L. M., Campbell, D. B., Hawke, B. R., Ghent, R. R. and Margot, J. L. 2006. *37th Annual Lunar and Planetary Science Conference, March 13-17, 2006, League City, Texas,* Abstract No. 1717.

Campbell, D.B., Campbell, B.A., Carter, L.M., Margot, J.L. and Stacy, N.J.S. 2006. No Evidence for Thick Deposits of Ice at the Lunar South Pole *Nature.* 443(7113):835-837.

Campbell, D.B and Carter, L.M. 2006. Earth Based Radar Imagery and Topography: Input to LCross Target Selection. URL: www.lpi.usra.edu/meetings/lcross2006/pdf/9002.pdf, (last date accessed: 7 January 2007)

Carlotto, M.J. 1996. *Shape from Shading*. URL: http://www.newfrontiersinscience.com/
martianenigmas/Articles/SFS/sfs.html, (last date accessed: 19 Feb. 2007)

Cherrington, E.H. 1984 (2d). *Exploring the Moon through Binoculars and Small Telescopes*. Dover.

Chevrel, S. and Legrand, M. 1994. Determining Heights. Section 4.5.2.2, Chap. 5, Vol 1. In Martinez, Patrick (ed). *The Observer's Guide to Astronomy*. Cambridge Univ. Press, New York City, New York. pp. 144-153

Chin, G., Bartels, A., Brylow, M., Foote, M., Garvin, J., Kaspar, J., Keller, J., Mitrofanov, I., Raney, K. and Robinson, M. et al. 2007. Update on the Lunar Reconnaissance Orbitor: The Instrument Suite and Mission. *38th Annual Lunar and Planetary Science Conference, March 12-16, 2007, League City, Texas,* Abstract No. 1764. URL: http://www.lpi.usra.edu/meetings/lpsc2007/pdf/1764.pdf (last date accessed 7 Feb. 2007)

Cook, A. C., Robinson, M. S. and Watters, T. R. 2000. Planet-wide Lunar Digital Elevation Model. *31st Annual Lunar and Planetary Science Conference, March 13-17, 2000, Houston, Texas*. Abstract No. 1978.

Cook, A. C., Spudis, P. D., Robinson, M. S., and Watters, T. R. 2002. Lunar Topography and Basins Mapped Using a Clementine Stereo Digital Elevation Model. *33rd Annual Lunar and Planetary Science Conference, March 11-15, 2002*. Abstract No. 1281.

Davies, M.E., Colvin, T.R., Meyer, D.L. and Nelson, S. 1994a. The Unified Lunar Control Network: 1994 Version. *J. Geophysical Res.* 99(E11):23,211-23,214

Davies, M.E., Colvin, T.R., Meyer, D.L. and Nelson, S. 1994b. The Unified Lunar Control Network: 1994 Version. (Datafile). URL: http://astrogeology.usgs.gov/Projects/LunarConsortium/data/topo_con/control.asc, (last date accessed: 7 January 2007)

Davis III, W.F. 1997. Determination of Lunar Elevations by the Shadow Method: Analysis and Improvements. URL: http://www.zone-vx.com/vertical-studies.pdf, (last date accessed: 7 January 2007).

Davis III, W.F. 1998. The Mountains of the Moon. *Sky & Telescope*. 96(5):114-118.

Elachi, C., Kobrick, M., Roth, L, Tiernan, M, and Brown, W. E., Jr. 1976. Local lunar topography from the Apollo 17 ALSE radar imagery and altimetry. *The Moon*. 15:119-131.

Ellison, D. Oct. 2, 2006. The Big Guns. URL: http://www.planetary.org/blog/article/00000710/, (last date accessed: 7 January 2007).

Evans, R. June 2006a. The Moon on a Spreadsheet: Photoclinometry using Excel. S*elenology Today*. 1:21-59

Evans, R.   June 2006b. *Excel Spreadsheets for SFS Photoclinometry*.   URL: http://digilander.libero.it/glrgroup/workbooks.zip, (last date accessed: 17 Feb. 2007)

Gaddis, L. R., Skinner, J. A., Jr., Hare, T., Tanaka, K., Hawke, B. R., Spudis, P., Bussey, B., Pieters, C., and Lawrence, D. 2006. The Lunar Geologic Mapping Program and Status of Copernicus Quadrangle Mapping. *37th Annual Lunar and Planetary Science Conference, March 13-17, 2006, League City, Texas,* Abstract No. 2135.

Griffin, M. (NASA). Oct. 3, 2006. Administrator's Remarks Before the 57th Annual International Astronautical Congress. URL: http://www.nasa.gov/pdf/159915main_IAC_Valencia%20-2006.pdf, (last date accessed: 7 January 2007).

Hale, W.S. and Head, J. W. 1979. Central Peaks in Lunar Craters: Morphology and Morphometry. *Lunar and Planetary Science X*, Proceedings. pp. 491-493.

Hale, W.S. and Grieve, R.A. F. 1982. Central Peak and Peak Ring Development: Constraints from Lunar Peak Volumes. *Lunar and Planetary Science XIII*, Proceedings. pp. 297-298.

Hapke, B. 1993. *Theory of relectance and emittance spectroscopy*. Cambridge Univ. Press, Cambridge, UK.

Heiken, G.H., Vaniman, D.T. and French, B.M. 1991. *Lunar Sourcebook - A User's Guide to the Moon.* Cambridge Univ. Press. Cambridge, England. Table 4.1.

Hiesinger, H. and Head III, J.W. 2006. New Views in Lunar Geoscience: An Introduction and Overview. In Jolliff, B.L. et al (eds). New Views of the Moon. *Reviews in Minerology & Geochemistry.* 60:1-81.

Honda, C., Morota, T., Yokota, Y., Haruyama, J., Ohtake, M., Matsunaga, T., Ogawa, Y., Demura, H., Hirata, N., Iwasaki, A., *et al.* 2007. Preliminary Test of Accuracy of Digital Terrain Model Derived from Selene/LISM/TC Data. *38th Annual Lunar and Planetary Science Conference, March 12-16, 2007, League City, Texas,* Abstract No. 1899. URL: http://www.lpi.usra.edu/meetings/lpsc2007/pdf/1899.pdf (last date accessed 7 Feb. 2007)

Jamieson, H.D. 1993. The Lunar Dome Survey - Fall, 1992 progress report. *J.A.L.P.O.* 37 (1):14-17.

Jamieson, H.D. 1997. Lunar Observer's Toolkit. URL: http://www.glrgroup.org/download/tool.exe, (last date accessed: 7 January 2007).

Jet Propulsion Laboratory. 2006. Biography of Dr. Charles Elachi, Director of JPL. URL: http://www.jpl.nasa.gov/bios/elachi/, (last date accessed 7 January 2007).

Kapral, C.A. and Garfinkle, R.A. 2005. GLR Lunar Domes Catalog, URL: http://www.glrgroup.org/domes/kapralcatalog.htm, (last date accessed: 7 January 2007).

Kirk, R.L., Barrett, J.N. and Soderblom, L.A. 2003. Photoclinometry Made Simple *Proceedings of the Conf. on Advances in Planetary Mapping, Houston, Texas, 2003*. URL: http://astrogeology.usgs.gov/Projects/ISPRS/MEETINGS/Houston2003/abstracts/Kirk_isprs_mar03.pdf, (last date accessed: 19 Feb. 2007)

Konopliv, A. S., Binder, A. B., Hood, L. L., Kucinskas, A. B., Sjogren, W. L. and Williams, J. G. 1998. Improved Gravity Field of the Moon from Lunar Prospector. *Science*. 281(5382): 1476.

Kopal, Z. 1962. Determination of Altitudes on the Moon. Part IV in Topography of the Moon. Chap. 7 in Kopal, Z. (ed). *Physics and Astronomy of the Moon*. Academic Press, New York, N.Y.

Koschny, D., Foing, B.H., Frew, D., Almeida, M., Sarkarati, M., Volp, J., Grande, M., Huovelin, J., Josset, J. L., Nathues, A. *et al.* 2007. SMART-1 Lunar Science Planning. *38th Annual Lunar and Planetary Science Conference, March 12-16, 2007, League City, Texas,* Abstract No. 1996. URL: http://www.lpi.usra.edu/meetings/lpsc2007/pdf/1996.pdf (last date accessed 7 Feb. 2007)

Kuiper, G.P. 1960. *Photographic Lunar Atlas*. Univ. of Chicago, Chicago, Illinois.

Kuiper, G.P. 1961. *Orthographic Atlas of the Moon*. Univ. of Ariz. Press, Tuscon, Arizona.

Law, N. M., Mackay, C. D. and Baldwin, J. E. 2006. Lucky Imaging: High Angular Resolution Imaging in the Visible from the Ground. *Astro. & Astrophysics*. 446(2):739-745.

Lemoine, F.G., Smith, D.E., Zuber, M.T., Neumann, G.A., and Rowlands, D.D. 1997. A 70th Degree Lunar Gravity Model (GLGM-2) from Clementine and other tracking data. *J. Geo. Res.* 102:16, 339-359.

Lena, R. 2006. Editorial. *Selenology Today.* 1:3-4

Lena, R., Pau, K.C., Phillips, J., Fattinnanzi, C., and Wöhler, C. 2006. Lunar Domes: A Generic Classification of the Dome near Valentine, Located at 10.26 E and 31.89 N. *JBAA.* 116(1):34-39. URL: http://www.glrgroup.org/domes/File0351/File0351.pdf, (date last accessed 12 Feb. 2007)

Lena, R., Wöhler, C., Bregante M.T., and Fattinnanzi, C. 2006. A Combined Morphometric and Spectrophotometric Study of the Complex Lunar Volcanic Region in the south of Petavius. *JRASC.* 100(1): 14-24. URL: http://www.christian-woehler.de/petavius_jrasc.pdf, (date last accessed 12 Feb. 2007)

Lena, R., Wöhler, C., Bregante, M. T., Phillips, J. , Zompatori, D., and Sbarufatti, G. 2007. Two Domes in Mare Fecunditatis near Messier Crater. *Selenology Today.* 3:25-37. URL: http://digidownload.libero.it/glrgroup/selenologytoday3.pdf, (date last accessed 12 Feb. 2007)

MacDonald, T.L. 1931. On the Determination of Relative Lunar Altitudes. *J.B.A.A.* 41:267-379.

Margot, J.L., Campbell, D.B., Jurgens, R.F., and Slade, M.A. 1999a. The Topography of Tycho Crater. *J. Geo. Res.* 104(E5):11875-11882.

Margot, J. L., Campbell, D. B., Jurgens, R. F., Slade, M. A. 1999b. Topography of the Lunar Poles from Radar Interferometry: A Survey of Cold Trap Locations. *Science.* 284(5420):1658-1660.

Margot, J.L., Campbell, D.B., Jurgens, R.F. and Slade, M.A. 2000. Digital Elevation Models of the Moon from Earth-Based Radar Interferometry. *IEEE Trans. on Geoscience and Remote Sensing.* 38 (2):1122-1133

McDowell, J. 2004. Lunar Nomenclature. URL: http://host.planet4589.org/astro/lunar/, (last date accessed 7 January 2007).

Mosher, J. and Bondo, H. 2006. Lunar Terminator Visualization Tool (LTVT) (software) URL: http://inet.uni2.dk/~d120588/henrik/jim_ltvt.html, (last date accessed 7 January 2007).

NASA. 1980. Lunar Topographic Orthophotomap (LTO) Series Apollo Photo and Map Index Map. URL: http://www.lpi.usra.edu/resources/mapcatalog/LTO/references.html, (last date accessed: 7 January 2007).

NASA. 2006a. Clementine Base Map Image Collections CL-3001 to CL-3015. URL: http://pds-imaging.jpl.nasa.gov/Admin/resources/cd_clementine.html#clmBASE, (last date accessed: 7 January 2007).

NASA. 2006b. Clementine HiRes Image Collections CL-4001 to CL-4078. URL: http://pds-imaging.jpl.nasa.gov/Admin/resources/cd_clementine.html#clmUVVIS, (last date accessed: 7 January 2007).

NASA. 2006c. Clementine Polar HiRes Image Collections CL-6001 to CL-6022. URL: http://pds-imaging.jpl.nasa.gov/Admin/resources/cd_clementine.html#clmHIRES, (last date accessed: 7 January 2007).

NASA. 2006d. NASA and Google to Bring Space Exploration Down to Earth. NASA Press Release 06_96AR. URL: http://www.nasa.gov/centers/ames/news/releases/2006/06_96AR.html, (last date accessed: 7 January 2007).

NASA and JPL. 2006. Planetary Data Systems Viewer Software Download Webpage. URL: http://pds.jpl.nasa.gov/tools/software_download.cfm, (last date accessed: 7 January 2007).

NASA and Washington Univ. in St. Louis. 2006a. Clementine Gravity and Topography Data Archive. Planetary Data Service Geosciences Node. (GLTM-2B digital elevation model). URL: http://pds-geosciences.wustl.edu/missions/clementine/gravtopo.html, (last date accessed: 7 January 2007).

NASA and Washington Univ. in St. Louis. 2006b. PDS Clementine Data Archive. Planetary Data Service Geosciences Node. URL: http://pds-geosciences.wustl.edu/missions/clementine/index.htm, (last date accessed: 7 January 2007).

Pike, R. J. 1976. Crater dimensions from Apollo data and supplemental sources. *The Moon*. 15:463-477.

Pike, R. J. 1977. Apparent depth/apparent diameter relation for lunar craters. *Lunar Sci. Conf., VIII, March 14-18, 1977, Proceedings. (Vol. 3).*

Rosiek, M. R., Archinal, B. A., Kirk, R. L., Becker, T. L., Weller, L., Redding, B., Howington-Kraus, E. and Galuszka, D. 2006. Utilization of Digitized Apollo and Lunar Orbiter Imagery for Mapping the Moon. *37th Annual Lunar and Planetary Science Conference, March 13-17, 2006, League City, Texas*, Abstract No. 2171

Rosiek, M.R., Cook, A.C., Robinson, M.S., Watters, T.R., Archinal, B.A., Kirk, R.L., and Barrett, J.M. 2007. A Revised Planet-Wide Digitial Elevation Model of the Moon. *38th Annual Lunar and Planetary Science Conference, March 12-16, 2007, League City, Texas,* Abstract No. 2297. URL: http://www.lpi.usra.edu/meetings/lpsc2007/pdf/2297.pdf (last date accessed 7 Feb. 2007)

Rosiek, M.R., Kirk, R. and Howington-Kraus, E. 2001. Combining Lunar Photogrammetric Topographic Data with Clementine LIDAR data. URL: http://astrogeology.usgs.gov/Projects/ISPRS/MEETINGS/Flagstaff2001/abstracts/isprs_etm_OCT01_rosiek_moon_topography.pdf, (last date accessed: 7 January 2007).

Rosiek, M. R., Kirk, R., and Howington-Kraus, E. 2002. Color-coded Topography and Shaded Relief Maps of the Lunar Hemispheres. *33rd Annual Lunar and Planetary Science Conference, March 11-15, 2002.* Abstract No. 1792.

Shaw, B., GLR Group. 2006. Lunar Dome Maps. URL: http://www.glrgroup.org/domes/domeatlas.htm, (last date accessed 12 February 2007).

Smith, D.E., Zuber, M.T., Neumann, G.A. and Lemoine, F.G. 1997. Topography of the Moon from the Clementine LIDAR. *J. Geo. Res.* 102:1591.

St. Clair, J. H., Carder, R. W., and Schimerman, L. A. 1979. United States Lunar Mapping - A Basis for and Result of Project Apollo. *Moon and the Planets*. 20:127-148.

Schimerman, L., U.S. Defense Mapping Agency. 1973. The Lunar Cartographic Dossier. NASA Pub. NASA-CR 1464000. URL: http://www.lpi.usra.edu/resources/mapcatalog/LTO/lto_references.pdf, (last date accessed: 7 January 2007).

Stacy, N. J. S., Campbell, D. B. and Ford, P. G. 1997. Arecibo radar mapping of the lunar poles: A search for ice deposits. *Science.* 276:1527-1530.

Thompson, T. W. 1979. A Review of Earth-based Radar Mapping of the Moon. *Moon and the Planets*. 20:179-198.

Tubbs, R. N. 2004. Lucky Exposures: Diffraction-Limited Astronomical Imaging through the Atmosphere. Ph.D dissertation. *The Observatory*. 124:159-160.

U.S. Air Force, NASA and Aeronautical Chart and Information Center. 1967. (1st Ed.) *Lunar Aeronautical Chart 112: Tycho*.

U.S. Defense Mapping Agency. 197_. NASA Lunar Topophotomap (TPM) series. URL: http://www.lpi.usra.edu/resources/mapcatalog/topophoto/, (last date accessed: 7 January 2007).

U.S. Defense Mapping Agency. 1974. NASA Lunar Topophotomap 41B4S1(50). URL: http://www.lpi.usra.edu/resources/mapcatalog/topophoto/41B4S1/, (last date accessed: 7 January 2007).

U.S. Defense Mapping Agency. 1974-1976. NASA Lunar Topographic Orthophotomap (LTO) Series Map. URL: http://www.lpi.usra.edu/resources/mapcatalog/LTO/, (last date accessed: 7 January 2007).

U.S. Defense Mapping Agency. 1975. NASA Lunar Topographic Orthophotomap LTO-41B4. URL: http://www.lpi.usra.edu/resources/mapcatalog/LTO/lto41b4_2/, (last date accessed: 7 January 2007).

U.S. Geological Survey (USGS). 2002. Lunar Clementine Globe (Petal Leaf Map). URL: http://astrogeology.usgs.gov/Gallery/MapsAndGlobes/moon.html#Globes, (last date accessed: 7 January 2007)

USGS. 2003. Color-Coded Topography and Shaded Relief Map of the Lunar Near Side and Far Side Hemispheres. Geologic Investigations Map Series I-2769. URL: http://geopubs.wr.usgs.gov/i-map/i2769/, (last date accessed: 7 January 2007)

USGS. 2006a. Clementine Map of the Topography of the Moon. In *The Clementine Mission*. URL: http://astrogeology.usgs.gov/Projects/Clementine/, (last date accessed: 7 January 2007)

USGS. 2006b. Gazetteer of Planetary Nomenclature. URL: http://planetarynames.wr.usgs.gov/jsp/FeatureTypes2.jsp?system=Earth&body=Moon&systemID=3&bodyID=11, (last date accessed 7 January 2007).

USGS. 2006c. Lunar Control Networks. URL: http://astrogeology.usgs.gov/Projects/ControlNetworks/Moon/, (last date accessed 7 January 2007).

USGS. 2006d. PDS Map-A-Planet Help Page: Data Sets. URL: http://pdsmaps.wr.usgs.gov/PDS/public/explorer/html/data_set.htm, (last date accessed 7 January 2007).

USGS. 2006e. Planetary Data Services Map-A-Planet Online Application: Moon. URL: http://pdsmaps.wr.usgs.gov/PDS/public/explorer/html/moonpick.htm, (last date accessed 7 January 2007).

USGS. 2006f. USGS Digital Data Viewer: dlgv32 Pro. (Software download website). URL: http://mcmcweb.er.usgs.gov/drc/dlgv32pro/, (date last accessed 3 Feb. 2007)

USGS. 2007. ISIS: Integrated Software for Imagers and Spectrometers. URL: http://isis.astrogeology.usgs.gov/, (last date accessed 19 Feb. 2007)

USGS, NASA and US Airforce ACIC. 197_. A Geologic Atlas of the Moon. URL: http://www.lpi.usra.edu/resources/mapcatalog/usgs/, (last date accessed 7 January 2007).

Viscardy, Georges. 1985. *Atlas-guide photographique de la lune: ouvrage de référence à haute résolution*. Masson.

Whitaker, E. A., Kuiper, G. P., and Hartmann, W. K. 1963. *Rectified Lunar Atlas*. Univ. of Ariz. Press. (NASA/ADS)

Westfall, John E. 2000. *Atlas of the Lunar Terminator*. Cambridge Univ. Press.

Wöhler, C. and Hafezi, K. 2005. A General Framework for Three-Dimensional Surface Reconstruction by Self-Consistent Fusion of Shading and Shadow Features. *Pattern Recognition*. 38 (7):965-983. URL: http://www.christian-woehler.de/woehler_hafezi_patrec.pdf, (date last accessed 12 Feb. 2007)

Wöhler, C., Lena, R. , Lazzarotti, P. , Phillips, J. , Wirths, M. and Pujic, Z. 2006. A Combined Spectrophotometric and Morphometric Study of the Lunar Mare Dome Fields Near Cauchy, Arago, Hortensius, and Milichius. *Icarus*. 183(2):237-264. URL: http://www.christian-woehler.de/lunar_domes_spectrophot_morph_icarus.pdf, (date last accessed 12 Feb. 2007)

Wöhler, C., Lena, R., Phillips, J., Bregante, M.T., Lazzarotti, P. and Sbarufattihristian, G. 2007. Vertical Studies about Rupes Bürg. *Selenology Today*. 3:65-78

Wood, C. A. 1973. Central Peak Heights and Crater Origins. *Icarus*. 20:503.

Wood, C.A. and Andersson, L.A. 1974. Lunar crater statistics - Earth face. (Unpublished).

Wood, C.A. 13 May 2004. A New/Old Catalog of Lunar Craters. *Lunar Picture of the Day (LPOD)*. URL: http://www.lpod.org/archive/archive/2004/05/LPOD-2004-05-13.htm, (last date accessed 7 January 2007).

Wood, C.A. 24 Dec. 2006. Measuring a Serpent. Lunar Picture of the Day. URL: http://www.lpod.org/?m=20061224, (last date accessed 7 January 2007).

Wood, C.A. and Andersson, L. 1978. New Morphometric Data for Fresh Lunar Craters. *Lunar and Planetary Science Conference, 9th, Houston, Tex., March 13-17, 1978, Proceedings*. New York, Pergamon Press, Inc., 1978, p. 3669-3689.

Yokota, Y., Haruyama, J., Ohtake, M., Matsunaga, T., Honda, C., Morota, T., Demura, H., Nirata, N. and LISM Working Group. 2007. Kilometer scale roughness analysis of lunar digital terrain model. *38th Annual Lunar and Planetary Science Conference, March 12-16, 2007, League City, Texas,* Abstract No. 2430. URL: http://www.lpi.usra.edu/meetings/lpsc2007/pdf/2430.pdf (last date accessed 7 Feb. 2007)

Zuber, M. T., Smith, D. E., Lemoine, F. G. and Neumann, G. A. 1994. The Shape and Internal Structure of the Moon from the Clementine Mission. *Science*. 266(5192):1839-1843.

Appendix – Description of Apollo era crater table digitization

A table craters and satellite feature names, positions and diameters was prepared from the online USGS Gazetteer of Planetary Nomenclature. Pike 1976 was reviewed. Where Pike's measurement corresponded to (1) the Gazetteer feature name and (2) the crater diameter was within 3 kilometers of the Gazetteer measurement, Pike's crater diameter, depth and peak height were digitized. Approximately 239 crater depths were digitized. Arthur 1974 was reviewed. Where Arthur's measurement corresponded to (1) the Gazetteer feature name and (2) the crater diameter was within 5 kilometers of the Gazetteer measurement, Arthur's crater diameter was digitized. Eleven craters from Elachi *et al.* 1976 and one measurement from Margot *et al.* 1999a were added. 37 central peak measurements from Wood 1973 were added.

This resulted in a table pairing the USGS Gazetteer lunar feature name, position, NCLN crater diameter with the crater diameter and depth from other higher accuracy Apollo era catalogue sources.

Next the initial digitization was filtered to exclude craters larger than 10 km in diameter where the diameter varied by more than 10% from the NCLN crater diameter.

The difference between the NCLN crater diameter and source catalogue diameters was computed (except for the list of central peaks from Wood 1973) in order to verify an association based on feature name and size. For craters over 10 kilometers in diameter, the criteria of a 10% difference was applied. For craters less then 10 kilometers in diameter, all craters were included because a criterion based on crater diameter difference was not statistically meaningful due to the whole number precision used in the GPN catalogue. The filter criteria excluded the measurement of Tycho from Margot *et al.* 1999a. In the final table, 91% of the craters have a diameter that differs from the GPN measurement by one kilometer or less. Examples of craters that meet the 10% difference criterion and also that have absolute crater diameter differences exceeding 10 kilometers are larger named craters such as Clavius, Hipparchus, Langrenus and Neper.

In the final table, 86% of craters have a diameter less than 20km, 11% between 50km and 20km, and 3% are larger than 50km in diameter. 50% have depths of less than 1km, 33% between 1 and 2km, 12% between 2 and 3km, and 4% greater than 3km.

Lunar domes classification and physical properties

By Raffaello Lena
Geologic Lunar Research (GLR) group

Abstract

This article provides an overview about the different classes lunar domes, physical properties of the magma and the geometry of the feeder dikes, and we derive a flow chart for dome classification which yields the same results as those obtained by using the classic principal component analysis (PCA). Moreover I describe the empirical relations between the inferred physical properties and the observed morphometric properties of the lunar domes. The purpose of this paper is two-fold: to perform classification of lunar domes using the derived flow chart and to compare the results in order to study which differences in the lunar interior may be responsible for the different lunar dome properties observed on the surface.

1. Introduction

Lunar domes are features with topography varying from circular to irregular outlines, have a common convex shape, and flank slopes generally less than 5°. Many domes have a crater pit or vent on their summit and are associated with the *maria* spectrally characterized by basaltic lavas. The lunar steep-sided Gruithuisen and

Mairan domes are morphologically and spectrally distinctive structures and appear similar to terrestrial features characterized by silicic viscous lavas (Wilson and Head, 2003; Chevrel et al., 1999, Head and Hess, 1978). Compositionally, these domes consist of an unusual variation of typical highland and mare soils.

Many telescopic observations have been made throughout the years and a large number of domes has been catalogued (Moore and Cattermole, 1957; Jamieson and Rae, 1965; Rae, 1963; Rae, 1966; Jamieson and Phillips, 1992). Kapral and Garfinkle (2005) have recently published a revised lunar dome catalogue. The term "lunar dome" has been used in the wide sense, so that lunar domes catalogues described also swellings on the mare, irregular swellings, and steep-sided hills, even though many of these structure may not be true volcanic domes.

Many theories have been put forward to explain the origin of lunar shields and domes but there is now a general consensus in interpreting most of them as magmatic features, extrusive (volcanic) or intrusive (laccolith) in nature. The most commonly used classification schemes for lunar domes are those introduced by Westfall (1964) and by Head and Gifford (1980). Both classification schemes are mainly based on a qualitative description of dome shape and its geologic setting rather than morphometric quantities. A novel classification scheme based on the spectral properties and three-dimensional shapes of the volcanic edifices was proposed by Wöhler et al. (2006) and is used also for recent studies about lunar domes (Lena et al., 2006a; Lena et al., 2006b; Lena et al., 2007b; Lena et al., 2007c).

The GLR scheme for dome classification

cf. Wöhler et al., 2006; Phillips and Lena, 2006) is based on the determination and evaluation of:
a) spectrophometric properties;
b) morphometric properties (diameters, heights, flank slopes, and volumes);
c) rheologic parameters, i. e. lava viscosity, effusion rate, and duration of the effusion process, determined by geophysical modelling.

Further studies carried out on additional dome fields containing effusive domes and more complex structures like those near Doppelmayer (Lena et al., 2007a), the Gruithuisen highland domes and the aligned domes in northern Mare Tranquillitatis (Wöhler et al., 2007), allowed the introduction of additional classes, also including volcanic construct with small diameters below 6 km and very low edifice volumes (< 1.2 km^3), which may represent intermediate objects between lunar domes and cones.

In this article i report a general overview about the physical properties of the magma that formed the domes as well as the geometry of the feeder dikes, and we will derive a flow chart for dome classification which results equivalent to those obtained by using the classical principal component analysis (PCA), described in detail in various works (cf. Pike, 1978, Wöhler et al., 2006). This scheme can be used for further investigation about the observed sizes and shapes of the lunar mare domes.

2. Eruption mechanisms required to develop lunar domes and their classification

The GLR classification scheme (Table 1) includes the following classes:

Class A domes are shallow, small domes formed by low viscosity lavas of high TiO_2 content erupting at high effusion rates over very short periods of time.

Class B_1 domes have steep flank slopes and formed from lavas of moderate TiO_2 content erupting at low to intermediate effusion rates over a long period of time.

Class B_2 domes formed during shorter periods of time than those of class B_1 resulting in shallow flanks with lower volumes.

Class C_1 domes have a low TiO_2 content and were formed by low viscosity lavas at high effusion rates resulting in large diameters and shallow flanks (pancake shapes).

Class C_2 domes are similar to C_1 but with high TiO_2 content in their soil.

Class D domes are very complex, large, shallow, voluminous domes such as Arago Alpha and Beta as well as several domes in the Marius Hills region, which likely formed during several stages of effusion.

Class E_1 domes have small diameters (< 6 km), flank slopes larger than 2°, low volumes and formed from lavas of moderate TiO_2 content erupting at low effusion rates.

Class E_2 domes have small diameters (< 6 km) formed by lava erupted at moderate effusion rates during shorter periods of time than those of class E_1, resulting in shallow flanks (< 2°).

Class G domes are large, steep and voluminous highland domes such as the

Table 1

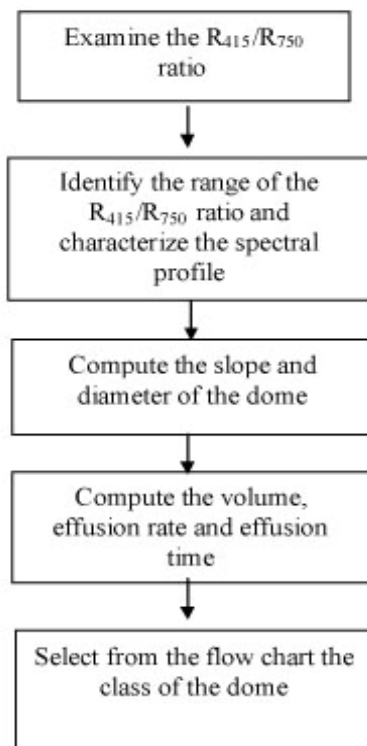| class	R_{415}/R_{750}	Slope [°]	D [km]	V [km³]	Effusion rate [m³ sec⁻¹]	Effusion time [years]
A	> 0.64	0.3-1.0	5-13	< 3	100-620	0.05-0.3
B_1	0.55-0.64	2.0-5.4	6-15	5-32	30-160	3.6-18
B_2	0.55-0.64	1.3-1.9	8-15	2-21	80-180	0.7-1.2
C_1	0.55-0.60	0.6-1.8	13-20	7-33	200-1000	0.06-7
C_2	0.60-0.64	1.0-2.5	8-17	4-17	100-220	0.6-6
E_1	0.58-0.62	2.0-4.0	<6	<1.2	≈ 25	1.0-1.6
E_2	0.58-0.62	<2.0	<6	<1.2	100-300	0.05-0.3
D	> 0.64	1.3-2.5	≈ 25	40-67		
G	0.55-0.60	> 6.0	7-30	20-390	48-120	12.8-42

Figure 1

page 64

Table 2 Magma physical properties

1.   temperature:

o increase in T => decrease in crystallization, atomic bonds and viscosity (η)

2. crystal content

o increase in crystal content => increase in viscosity (η)

3. silica content (SiO_2):

o increase in SiO_2 => increase in viscosity (η)

4. pressure (P):

o increase in P => decrease in viscosity (η), not a steady rate: associate with mineral phase changes and/or changes in the structure of the melt

5. density (ρ)

o increase in T => decrease in density

o varies with composition

o increase in P => increase in density (minor variation with temperature)

6. rheology

 different flow regimes depending on magma rise speed (U), dike depth (L) and viscosity (η)

o laminar: particles in the fluid all move with a constant velocity and direction

o turbulent: particles become highly disorganized with variable speeds and

directions.

Relationship of magma rise speed (U), dike depth (L) and viscosity (η) is expressed by Reynold's Number (Re):

$Re = U L / \eta k$

If Re > 1000-2000 there is laminar flow transitions to turbulent.

Silicic lavas have low magma rise speed (U) and high viscosities => low Reynold's Numbers (flow laminarly).

More mafic lavas have higher magma rise speed (U) and lower viscosities =>higher Reynold's Numbers (but still laminar flows).

7. Effect temperature T on viscosity η (the Arrhenian model)

$\eta = \eta_0 \exp [(Ea + pVa) / RT]$

where η is viscosity, η_0 the asymptotic viscosity at infinite temperature, Ea the activation energy of a viscous flow, which is constant for an Arrhenian fluid , Va the activation volume for a viscous flow and R the gas constant.

Gruithuisen and Mairan domes.

One of the problems of classifying lunar domes is that they cannot all be classified sensibly by using only one parameter. For example, the modal parameters required to adequately define highland domes (e. g. the Gruithuisen domes) are very different from those required to define a typical mare dome which can be formed by lavas of different TiO_2 content, as shown from the R_{415}/R_{750} ratio.

Albedo at 750 nm is an indicator of variations in soil composition, maturity, particle size, and viewing geometry. The R_{415}/R_{750} colour ratio essentially is a measure for the TiO_2 content of mature basaltic soils, where high R_{415}/R_{750} ratios correspond to high TiO_2 content and vice versa (Charette et al., 1974). However, for many lunar regions the relation between R_{415}/R_{750} ratio and TiO_2 content displays a significant scatter (Gillis and Lucey, 2005). The R_{950}/R_{750} colour ratio is related to the strength of the mafic absorption band, representing a measure for the FeO content of the soil, and is also sensitive to the optical maturity of mare and highland materials (Lucey et al., 1998).

Further criteria apart from spectral data have to be taken into account for a classification scheme. Principal criteria are:

a) the physical magma properties;
b) the effect of stress fields induced by the major basin impacts.

A synthesis of the physical magma properties are given in Table 2. They are related to soil composition, viscosity η, yielding a measure for the fluidity of the erupted lava, and crystal content. Chemical composition (e. g. silicic or basaltic lavas) and crystal content affect the magma viscosity, where more silicic composition and higher crystal content, also due to a lower temperature, will increase the viscosity. The magma viscosity η influences the morphology of the volcanic edifices (slope, diameter, edifice volume) but also the rheologic properties and the style of eruption. The rheologic properties are essentially related to the effusion rate E, i. e. the lava volume erupted per second, the magma rise speed U, and the duration T of the effusion process.

Wilson and Head (2003) provide a quantitative treatment of dome-forming eruptions. Their model estimates the yield strength τ, i. e. the pressure or stress that must be exceeded for the lava to flow, the plastic viscosity η, the effusion rate E, and the duration T = V/E of the effusion process, where V denotes the dome volume.

Studies carried out about the ascent and eruption of mare basalts suggest that domes may be the result of dikes rising from melt reservoirs in the lunar mantle or crust (Head and Wilson, 1996). Moreover, the stress state of the lunar lithosphere is likely to be important in assessing the volume of magma, both erupted and intruded in a specific lunar region, including the eruption mechanisms required to develop the volcanic construct and its associated structures, the depth of magma source, the depth of upper dike tip and the width of dike (Scott and Wilson, 2001).

Magma ascent is related to impact-induced fracture and fault zones, with the location of conduits having been affected by impact structures, or it may

result from the reactivation of pre-existing pre-Imbrian faults produced by the impact that formed the Imbrium basin. Ascending magmas preferentially extrude to the surface where the crust is thin, i. e. on the lunar nearside or in the impact basins. On the farside the crustal thickness is larger and therefore the magmas stalled and cooled in dikes before they reached the surface. On the basis of these studies (Scott and Wilson, 2001; Head and Wilson, 1996; Yingst and Head, 1997) it can be concluded that in areas with a thinner crust dikes could still reach the surface later in lunar history whereas in other regions the dikes stalled in the crust and could not propagate to the surface.

3. Determining the dome class

To determine the class of a dome, the three spectral features R_{750}, R_{415}/R_{750}, and R_{950}/R_{750} along with the morphometric features such as flank slope, diameter, height, edifice volume and form factor are used for a principal component analysis (PCA).

Domes belonging to the same cluster share certain characteristic spectral and morphometric properties. Refer to the works of Pike (1978) and Wöhler et al. (2006) for a source of the principal component analysis (PCA).

As shown in Table 1, Class A domes display small to moderate diameters between 5 and 13 km with very low flank slopes and volumes and were formed by spectrally strongly blue lavas of high R_{415}/R_{750} spectral ratio. Class B domes have small to moderate diameters between 6 and 15 km and were formed from lavas of low to moderate R_{415}/R_{750} spectral ratio. Steep and voluminous
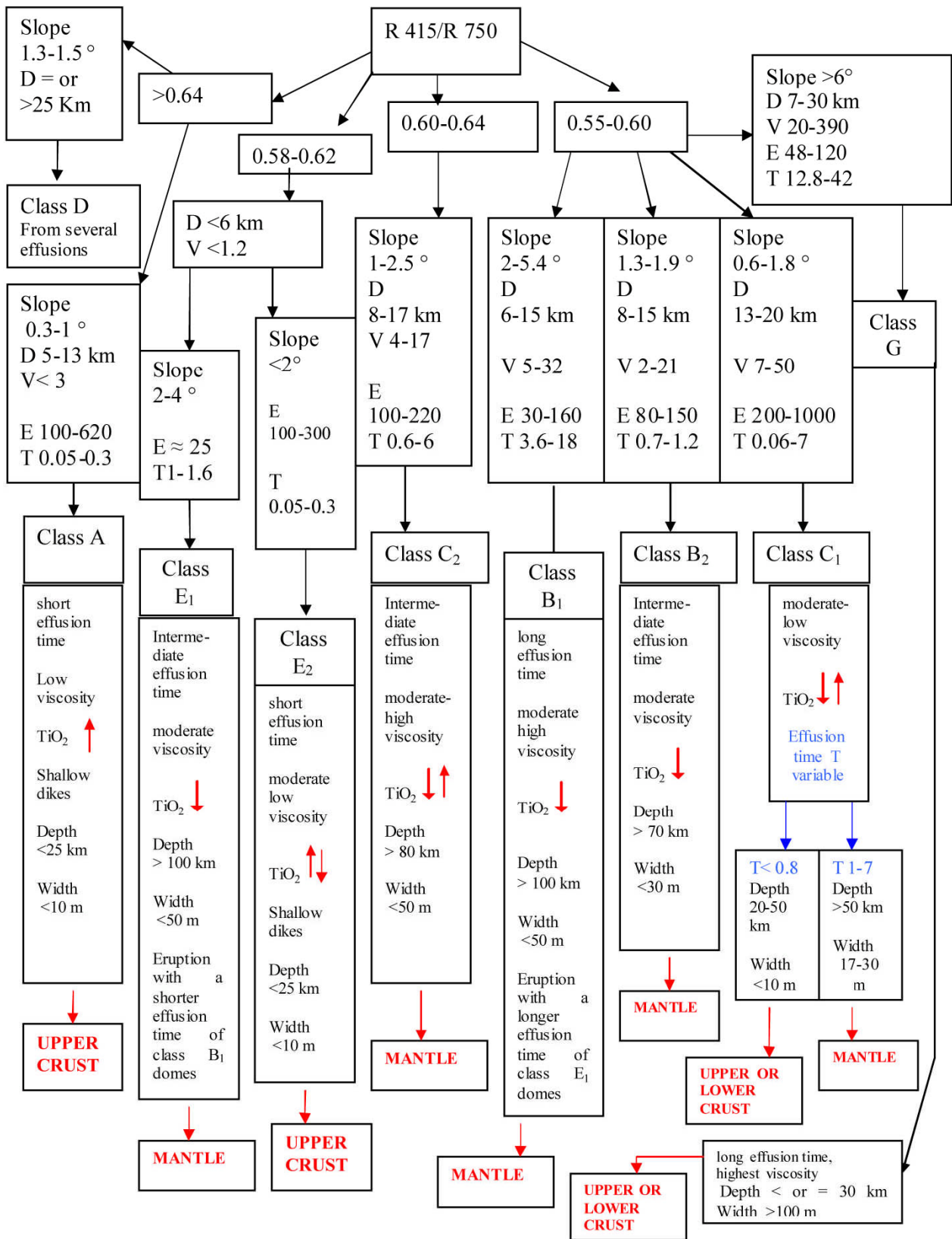
class B domes with flank slopes larger than 2° are assigned to subclass B_1 while the lower edifices with flank slopes below 2° make up subclass B_2. Class C domes are larger (diameter between 8 and 20 km) with relatively low flank slopes below 2°. Edifices formed from spectrally red lavas of low to moderate R_{415}/R_{750} ratio, having large diameters between 13 and 20 km and large edifice volumes of several tens of km^3 are assigned to subclass C_1, while spectrally bluer domes of moderate to high R_{415}/R_{750} ratio, smaller diameters between 8 and 17 km, and lower edifice volumes of less than 17 km^3 are assigned to subclass C_2. A further class is made up by domes with small diameters below 6 km and very low edifice volumes below 1.2 km^3. This group is further subdivided into class E_1 and E_2, denoting the steep-sided (flank slope > 2°) and the shallow edifices (flank slope < 2°).

As a first step in classification, several parameters have to be computed, each of which is applicable to a certain group of domes, e. g. slope, diameter, effusion rate etc. To do this in a consistent manner, a hierarchy of parameters should be chosen. The stepwise scheme to design a dome class is summarized in Fig.1. The use of a flow chart yields the same class assignment of the examined domes without the use of the principal component analysis (PCA). The sequence of dome classes and their assignment is shown diagrammatically on the flow chart proposed in Fig.2.

4. Discussion

According to the flow chart shown in Fig. 2 it is possible to derive discriminative criteria for "similar"

Figure 2 Flow Chart and dome classification scheme

Slope 1.3-1.5 ° D = or >25 Km

R 415/R 750

>0.64

Slope >6° D 7-30 km V 20-390 E 48-120 T 12.8-42

0.60-0.64

0.55-0.60

0.58-0.62

Class D From several effusions

D <6 km V <1.2

Slope 1-2.5 ° D 8-17 km V 4-17 E 100-220 T 0.6-6

Slope 2-5.4 ° D 6-15 km V 5-32 E 30-160 T 3.6-18

Slope 1.3-1.9 ° D 8-15 km V 2-21 E 80-150 T 0.7-1.2

Slope 0.6-1.8 ° D 13-20 km V 7-50 E 200-1000 T 0.06-7

Class G

Slope 0.3-1 ° D 5-13 km V< 3 E 100-620 T 0.05-0.3

Slope 2-4 ° E ≈ 25 T1-1.6

Slope <2° E 100-300 T 0.05-0.3

Class A

Class E₁

Class E₂

Class C₂

Class B₁

Class B₂

Class C₁

short effusion time

Low viscosity

TiO₂ ↑

Shallow dikes

Depth <25 km

Width <10 m

UPPER CRUST

Interme-diate effusion time

moderate viscosity

TiO₂ ↓

Depth > 100 km

Width <50 m

Eruption with a shorter effusion time of class B₁ domes

MANTLE

short effusion time

moderate low viscosity

TiO₂ ↑↓

Shallow dikes

Depth <25 km

Width <10 m

UPPER CRUST

Interme-diate effusion time

moderate-high viscosity

TiO₂ ↓↑

Depth > 80 km

Width <50 m

MANTLE

long effusion time

moderate high viscosity

TiO₂ ↓

Depth > 100 km

Width <50 m

Eruption with a longer effusion time of class E₁ domes

MANTLE

UPPER OR LOWER CRUST

Interme-diate effusion time

moderate viscosity

TiO₂ ↓

Depth > 70 km

Width <30 m

MANTLE

moderate-low viscosity

TiO₂ ↓↑

Effusion time T variable

T< 0.8 Depth 20-50 km Width <10 m

T 1-7 Depth >50 km Width 17-30 m

UPPER OR LOWER CRUST

MANTLE

long effusion time, highest viscosity Depth < or = 30 km Width >100 m

classes (e. g. B_2 and C_1). The conditions under which domes of classes B_2 and C_1 formed were very similar, except that in the case of the C_1 domes the effusion rates were much higher. In this scenario, the influence of the impact-induced stress fields was that magma flow through the crust was easier for the class C_1 domes, while the magma properties themselves (composition, viscosity, crystal content) were not perceivably different. Between classes B_1 and E_1, the discriminative criterion is the effusion time but not the flank slope, since the duration of the effusion process was longer for class B_1 domes. Between A and E_2, the most important discriminative parameter is the spectral appearance (higher R_{415}/R_{750} ratio and thus higher TiO_2 content for class A) and not primarily the morphometric and rheologic properties.

In the flow chart, the duration T of the effusion process is an important discriminative parameter, which appears to have a major effect on the volcanic construct and also reflects the rheologic conditions valid during the dome formation. It can be classified as:

A) very short durations << 1 year of the effusion process (between 2 and 10 weeks), typical of classes A, E_2 and some domes of Class C_1

B) intermediate durations between less than 1 year and 3 years (classes B_2, C_2, C_1, E_1)

C) long duration of the effusion process reaching values as high as 18 years (typical of class B_1 domes), where for the highland domes (class G) it can be comprised between 12 and 45 years.

Mare volcanic eruptions are fed from source regions at the base of the crust or deeper in the lunar mantle. According to Wilson and Head (1996), some dikes intruded into the lower crust while others penetrated to the surface, being the sources for extensive outpourings of lava. Thus the surface manifestation of dike emplacement in the crust is depending on the depth below the surface to which the dike penetrates. Wilson and Head (1996) state that if a dike does not propagate near the surface but stalls at greater depth, the strain will be insufficient to cause any dislocation near the surface. If a dike propagates at intermediate depths the strain will cause extensional deformation, eventually leading to graben formation. On the contrary, if a dike propagates at shallow depth and gains surface access at some points, a subsequent lava effusion will occur and the surface manifestation of the dike will be a fracture. Depending on the magma density relative to the density of the crust and the mantle, and also on the stress state of the lithosphere, some dikes erupt at the surface while others penetrate to depths shallow enough to produce linear graben.

Several studies have been carried out about the geometry of dikes rising from melt reservoirs in the lunar mantle or crust (Head and Wilson, 1996) and the assessment of the rheologic properties of the lavas related to magma rise speed U, dike width W, and dike length L (cf. Lena et al., 2007; Wöhler et al., 2007). In the scenario of dikes producing effusion of lava, an important parameter is the effusion time T related to the magma rise speed U at which the dike propagates. The magma rise speed U,
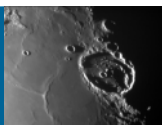
the dike geometry defined by its width W and length L, and the eruption rate E are related by

$$E = UWL \qquad (1)$$

where L and W are not independent. A detailed viscoelastic model for the dependence between lava viscosity and the ratio L/W is suggested by Rubin (1993a). Based on this model, Wilson and Head (2003) derive a value of L/W= 200 for the Gruithuisen domes. Accordingly, a higher magma rise speed U, which is due to lower magma viscosity, is possible for lower values of W and L, given the effusion rate E. According to Jackson et al. (1997), if it is assumed that the length of a dike approximately equals its vertical extension, domes formed by high magma rise speed U originated from reservoirs located at shallow depth and with narrow dike width.

Moreover, the effusion time T, edifice volume V, and the effusion rate E are related by

$$T = V/E \qquad (2)$$

Hence, a short effusion time is due to a high magma rise speed U in dikes that originate at shallow depths, yielding low edifice volumes. Numerical modelling

of magma ascent and dikes geometry is described in a recent paper by Wöhler et al. (2007). The diagrams shown in Figs. 3-6 report the dependence of dike width W and dike length/depth L on the effusion time T of the examined classes of domes (Table 1), along the region where some dome classes overlap. From Figs. 3 and 4 several conclusions can be drawn:

1) Very short durations << 1 year of the effusion process (classes A, E_2, and some domes of Class C_1) are associated with narrow dikes (width < 10 m).

2) Intermediate durations between less than 1 year and 3 years (classes B_2, C_2, C_1, and E_1) are associated with dike of width between 10 and 90 m.

3) Long durations of the effusion process reaching values as high as 18 years (class B_1 domes) are associated with dikes of widths between 10 and 90 m. For the highland domes (class G), long effusion times (between 12 and 45 years) are associated with dikes of widths between 100 and 200 m, demonstrating their unusual character and origin: volcanic constructs formed by viscous lavas of more silicic composition (Chevrel et all, 1999). Figs. 5 and 6 show the approximate location of the magma source relative to the average thicknesses of the lunar crust and mantle. Wieczorek et al. (2006) obtain thicknesses of the upper crust of 22 km and 32 km and total crustal thicknesses of 50 km and 55 km for the Hortensius/Milichius/T. Mayer region and northern Mare Tranquillitatis, respectively. On the average, the crust of
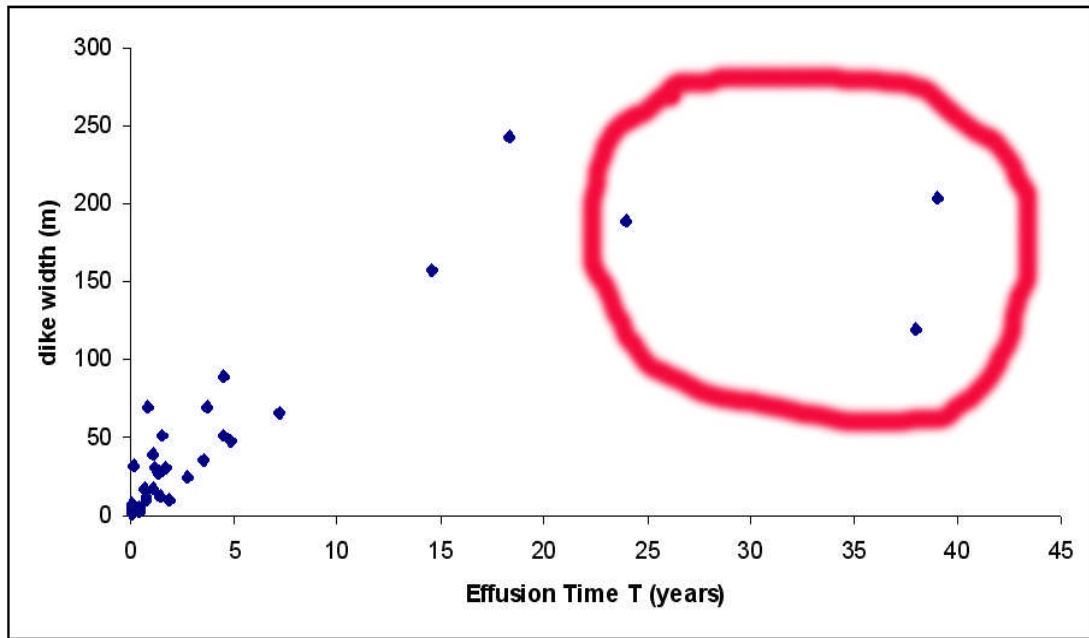
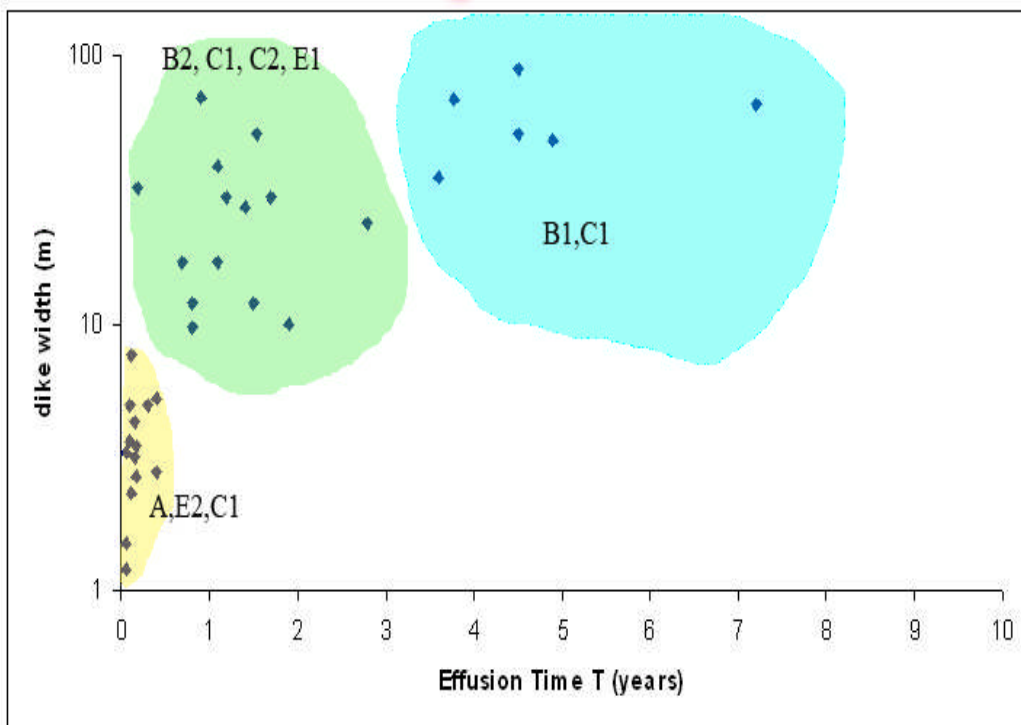Figure 3. Dependence of dike width W on effusion time T. The red circle in the diagram indicates the highland domes.

Figure 4. Dependence of dike width W (log scale) on effusion time T. The colour circles in the diagram indicate the distribution of domes classes in the GLR classification scheme.
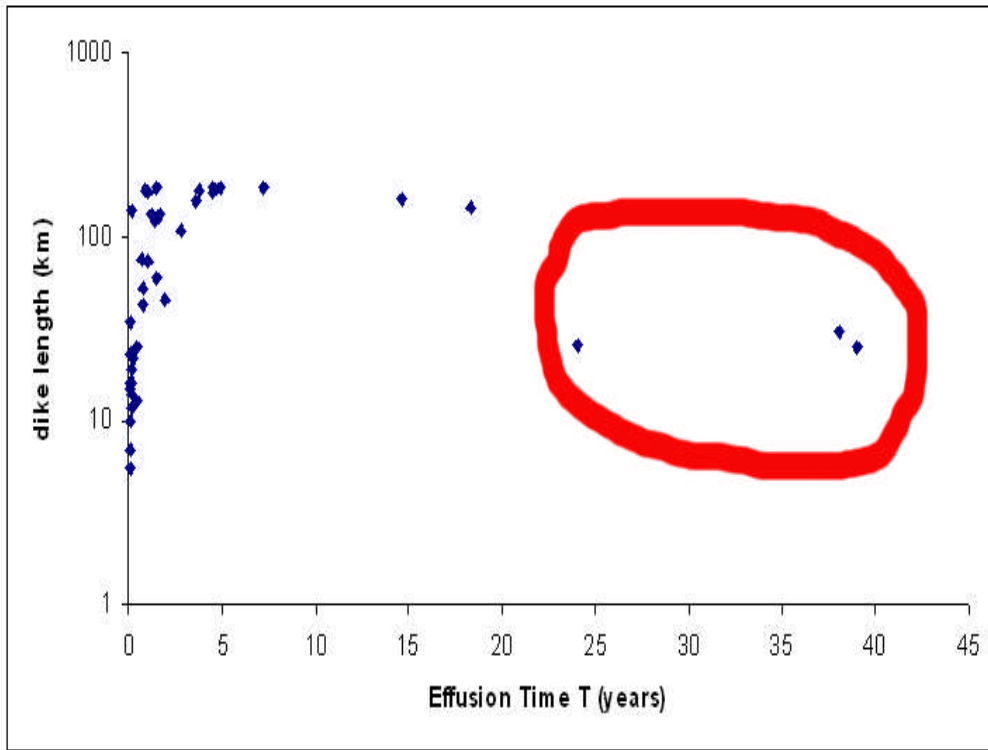
Figure 5a. Dependence of dike length /depth L
(log scale) on effusion time T. The red circle
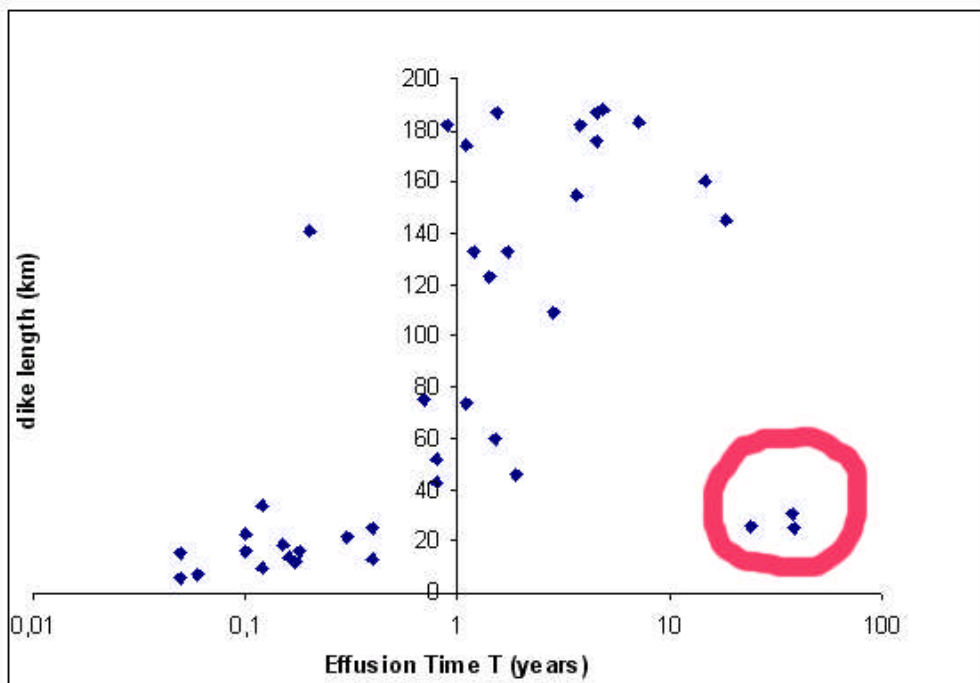in the diagram indicates the highland domes.

Figure 5b. Dependence of dike length /depth L
(log scale) on effusion time T (log scale). The red
circle in the diagram indicates the highland domes.

the Moon is about 50 km thick, although this value is uncertain by about ±15 km (Wieczorek et al., 2001; Wieczorek et al., 2006). Based on the flow chart of Figs. 2 and 7 the following conclusions can be drawn:

a) Very short durations << 1 year of the effusion process (classes A, E_2 and some domes of class C_1) are associated with dike depths between 6 and 25-30 km (comprised in the upper crust). Hence, class A domes are characterized by more fluid lavas, possibly associated with a higher temperature of the erupting lavas and a somewhat higher TiO_2 content than E_2 domes. Due to the broad range for Class C_1, we can divide this class into domes formed at short (T < 0.8 years) and intermediate effusion time (T between 1 and 7 years). In the first case (see Fig. 2), domes are associated with magma reservoirs comprised in the upper or lower crust and possibly with higher temperature of the erupting lavas. In the second case, the domes originated from magma reservoirs deep in the mantle and with lower temperature, yielding a moderate viscosity.

b) Intermediate durations between less than 1 year and 3 years (classes B_2, C_2, C_1, E_1) are associated with dike depths between 30 and 55 km (comprised in the lower crust) and between 70 and 190 km (well below the crust, in the mantle). Domes of classes B_2, C_2, and E_1 originate from lavas of moderate viscosity while the steeper edifices of class E_1 presumably built up at decreasing eruption rates ascribed to the lowering of the temperature during

ascent.

c) Long duration of the effusion process reaching values as high as 18 years (class B_1 domes) are associated with dike depths of about 100 km, i. e. in the mantle. They formed from high viscosity lavas during longer episodes of lava effusion than the class E_1 domes. Steeper edifices of class B_1 and E_1 have been produced by lower fluxes at cooler temperature and increased crystallisation during magma ascent.

According to the different character of the highland domes (class G), they originated at depths of about 25-30 km in the lower crust from dikes of large width and lavas of exceptionally high viscosity. Fig. 7 shows the dependence between the depth of the magma reservoirs and the shapes of the lunar domes according to the GLR classification scheme.

Temperature has a strong influence on lava viscosity. As temperature increases, viscosity decreases. For a temperature above the liquidus temperature, magma viscosity is commonly described in terms of the Arrhenian model (see Table 2). An initially fluid pure melt that segregates from its source region becomes an increasingly viscous, crystal-rich fluid as it cools down while approaching the surface. At subliquidus magma temperatures, viscosity strongly increases due to the increase of crystallinity and the change of melt composition as a result of crystallisation. Hence crystallisation is favoured by a low magma rise speed at depth magma reservoirs. In the case of the lunar domes the temperature will influence the
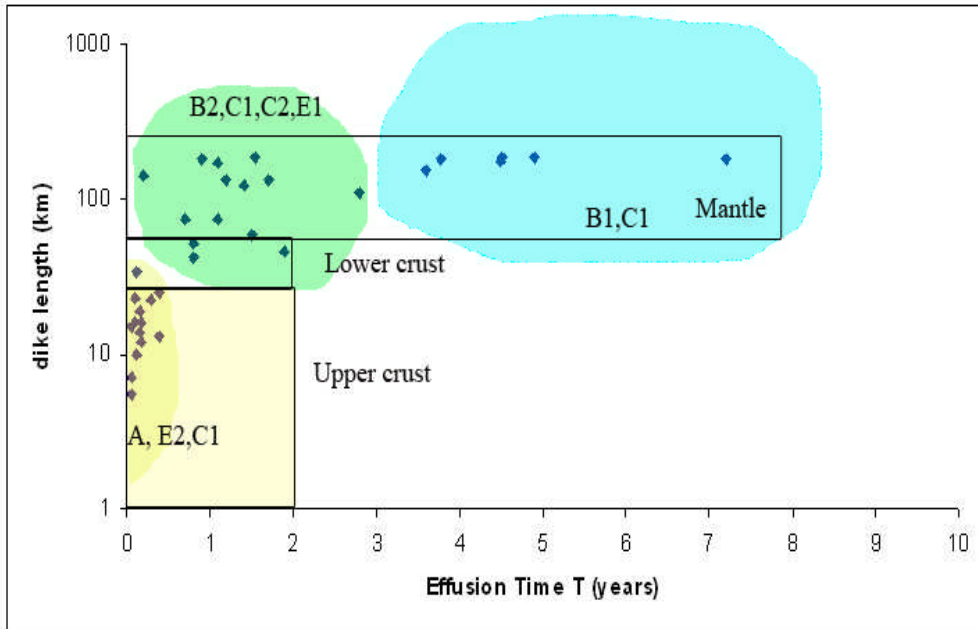
Figure 6a. Dependence of dike length /depth L (log
scale) on effusion time T. The colour circles
in the diagram indicate the distribution of domes
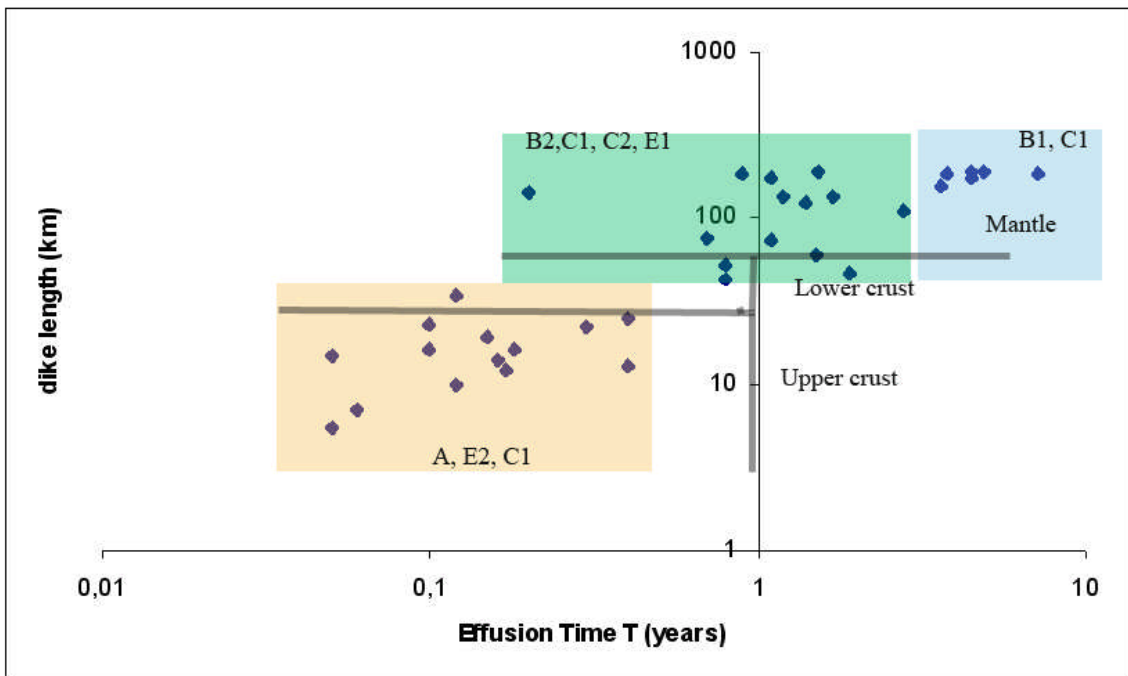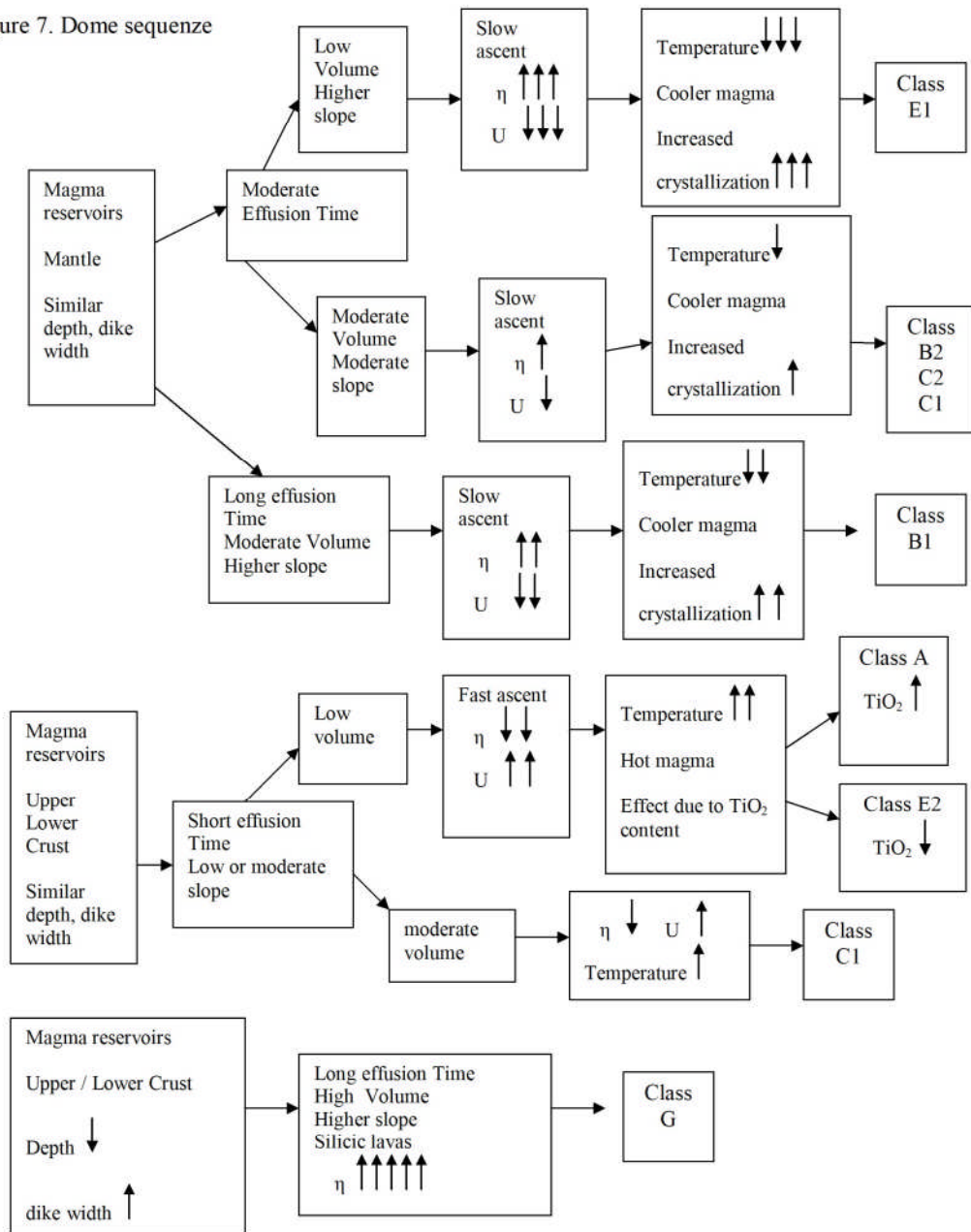classes in the GLR classification scheme.

Figure 6b. Dependence of dike length /depth L (log
scale) on effusion time T (log scale). The colour
circles in the diagram indicate the distribution of
domes classes in the GLR classification scheme.

Figure 7. Dome sequenze

"sequence" of the volcanic construct. In this scenario we interpret the different shapes of domes (and their different classification) as an effect related to the magma temperature reaching the surface, implying cooling of magma in the following order: B_2, C_2, C_1 => B_1 => E_1 (for magma reservoirs in the mantle located at similar depths and dike widths). For magma reservoirs in the crust (with similar depths and dike widths) the different "evolution" is related to the effect of high temperature and lower viscosity, which is influenced by higher TiO_2 content for Class A domes. The influence of lava temperature and viscosity will affect the shapes and morphometric properties of the domes of classes A, E_2 and C_1.

We have examined for a variety of lunar mare domes the relationship between the conditions in the magma source regions and the resulting eruption conditions at the surface. The proposed flow chart can be used for further investigation about the observed sizes and shapes of lunar mare domes.

Acknowlegdements: Many thanks to C. Wöhler for the interesting discussions about domes and shared studies between the conditions in the magma source regions and the resulting eruption conditions at the surface. Moreover for his critical reading of the manuscript.

References

[1] Charette, M. P., McCord, T. B., Pieters, C. M., Adams, J. B., 1974. Application of remote spectral reflectance measurements to lunar geology classification and determination of titanium content of lunar soils. J. Geophys. Res. 79, pp. 1605-1613.

[2] Chevrel, S. D., Pinet, P. C., Head, J. W., 1999. Gruithuisen domes region: A candidate for an extended nonmare volcanism unit on the Moon. J. Geophys. Res. 104(E7), pp. 16515-16529.

[3] Gillis, J. J., Lucey, P. G., 2005. Evidence that UVVIS ratio is not a simple linear function of TiO2 content for lunar mare basalts. Lunar Planet. Sci. XXXVI, abstract #2252.

[4] Head, J. W., Wilson, L., 1996. Lunar linear rilles as surface manifestation of dikes:predictions and observations. Lunar Planet. Sci. XXVII, abstract #519.

[5] Head, J. W., Gifford, A., 1980. Lunar mare domes: classification and modes of origin. The Moon and Planets 22, pp. 235-257.

[6] Head, J. W., Hess, P., 1978. Geologic characteristics of lunar highland volcanic domes (Gruithuisen and Mairan region) and possible eruption conditions. Lunar Planet. Sci. IX, pp. 488-490.

[7] Jackson, P. A., Wilson, L., Head, J. W., 1997. The use of magnetic signatures in identifying shallow intrusions on the moon. Lunar Planet. Sci. XXVIII, abstract #1429.

[8] Jamieson, H.D. and Rae, W.L.; 1965. The Joint A.L.P.O.-B.A.A. Dome Project. J. Brit. Astron. Assoc., Vol. 75, pp. 310-314.

[9] Kapral, C., Garfinkle, R., 2005. GLR Lunar Dome Catalog. http://www.glrgroup.org/domes/kapralcatalog.htm

[10] Lena, R, Wöhler, C., Phillips, J., Wirths, M., Bregante, M.T., 2007a. Lunar domes in Doppelmayer region: spectrophotometry, morphometry, rheology and eruption conditions. Planetary and Space Science In Press (DOI doi:10.1016/j.pss.2007.01.007).

[11] Lena, R, Wöhler, C., Pau, K.C, Bregante, M.T., 2007b. A study about the Manilius region and a dome located at 8.26° E and 10.52° N. Selenology Today, 3, pp. 9-24.

[12] Lena, R, Wöhler, C., Bregante, M.T., Phillips, J., Zompatori, D, Sbarufatti, G. 2007c. Two domes in Mare Fecunditatis near Messier. Selenology Today, 3, pp. 25-37.

[13] Lena, R., Wöhler, C., Phillips, J., Bregante, M. T., 2006a. The Hortensius Milichius-Tobias Mayer region: An unlisted dome located at 25.17°W and 6.07° N. Selenology Today 1, 4-10.

[14] Lena, R., Wöhler, C., Wöhler, A., Phillips, J., Pau, K. C., Lazzarotti, P., Bregante, M. T., 2006b. A study about two unlisted domes near Promontorium Laplace. Selenology Today 1, 11-17.

[15] Lucey, P. G., Blewett, D. T., Hawke, B. R. 1998. Mapping the FeO and TiO2 content of the lunar surface with multispectral imagery. J. Geophys. Res. 103(E2), pp. 3679-3699.

[16] Moore, P. and Cattermole, P. J., 1957. A Catalog of Lunar Domes. Parts 1-4, Internat. Lunar Soc., Vol 1.

[17] Phillips, J., Lena, R., 2006. New spectrophotometric and morphometric lunar dome classification. Selenology Today, 1, pp. 18-20.

[18] Pike,R.J.,1978.Volcanoes on the inner planets: Some preliminary comparisons of gross topography. LunarPlanet.Sci.IX, pp. 3239–3273.

[19] Rae, W.L.; 1963. J. Brit. Astron. Assoc., Vol. 73, pp. 169-175.

[20] Rae, W.L.; 1966. J. Brit. Astron. Assoc., Vol. 76, pp. 319-327.

[21] Rubin, A. S., 1993. Dikes vs. diapirs in viscoelastic rock. Earth and Planet. Sci. Lett. 199, pp. 641-659.

[22] Scott, R. S., Wilson, L., 2001. The stress state of the lunar lithosphere and the volumes of intruded and erupted magmas. Lunar Planet. Sci. XXXII, abstract #1549.

[23] Weitz, C. M, Head, J. W., 1999. Spectral properties of the Marius hills volcanic complex and implication for the formation of lunar domes and cones. J. Geophys. Res. 104(E8), pp. 18933-18956.

[24] Westfall, J.E 1964. A Generic Classification of Lunar Domes. J. Ass Lunar Planet. Obs., Vol. 18, No. 1-2, pp. 15-20.

[25] Wieczorek, M. A., Zuber, M. T., Phillips, R. J., 2001. The role of magma buoyancy on the eruption of lunar basalts. Earth and Planet. Sci. Lett. 185, pp. 71-83.

[26] Wieczorek, M. A., Jollis, B. A., Khan, A., Pritchard, M. E., Weiss, B. P., Williams, J. G., Hood, L. L., Righter, K., Neal, C. R., Shearer, C. K., McCallum, I. S.,Tompkins, S., Hawke, B. R., Peterson, C., Gillis, J. J., Bussey, B., 2006. The Constitution and Structure of the Lunar Interior. Rev. Mineralogy and Geochemistry. 60, pp. 221-364.

[27] Wilson, L., Head, J. W., 1996. Lunar Linear Rilles as Surface Manifestations of Dikes: Theoretical Considerations. Lunar Planet. Sci. XXVII, 1445.

[28] Wilson, L., Head, J. W., 2003. Lunar Gruithuisen and Mairan domes: Rheology and mode of emplacement. J. Geophys. Res. 108(E2), pp. 5012-5018.

[29] Wöhler, C., Lena, R., Lazzarotti, P., Phillips, J., Wirths, M., Pujic, Z., 2006. A combined spectrophotometric and morphometric study of the lunar mare dome elds near Cauchy, Arago, Hortensius, and Milichius. Icarus 183, pp. 237-264.

[30] Wöhler, C., Lena, R., Phillips, J., 2007. Formation of lunar mare domes along crustal fractures: rheologic conditions, dimension of feeder dikes, and the role of magma evolution. Icarus, in press.

[31] Yingst, R.A., Head, J.W.,1997.Volumes of lunar lava ponds in SouthPole-Aitken and Orientale basins:Implications for eruption conditions, transport mechanism, and magma source regions. J. Geophys. Res. 102, pp. 10909-10931.